Structure-activity studies of 1,2,4-oxadiazoles for the inhibition of the NAD$^+$-dependent lysine deacylase Sirtuin2

A. Colcerasa,[a] F. Friedrich,[a] J. Melesina,[b] P. Moser,[a] A. Vogelmann,[a,g] P. Tzortzoglou,[a] E. Neuwirt,[c] M. Sum[d] L. Zhang,[e] E. Ramos-Morales,[f] C. Romier,[f] O. Einsle,[e] E. Metzger[d], R. Schüle,[d,g] O. Groß,[c] W. Sippl [b] and M. Jung[*a, g]*

[a] *Institute of Pharmaceutical Sciences, University of Freiburg, Albertstraße 25, 79104 Freiburg, Germany*

[b] *Department of Medicinal Chemistry, Institute of Pharmacy, Martin Luther University of Halle-Wittenberg, 06120 Halle/Saale, Germany*

[c] *Institute of Neuropathology, Medical Center – University of Freiburg, Faculty of Medicine, University of Freiburg, 79106 Freiburg, Germany*

[d] *Department of Urology and Center for Clinical Research, University of Freiburg Medical Center, Breisacher Straße 66, 79106 Freiburg, Germany*

[e] *Institute of Biochemistry, University of Freiburg, Albertstraße 21, 79104 Freiburg, Germany*

[f] *Institut de Génétique et de Biologie Moléculaire et Cellulaire (IGBMC), Université de Strasbourg, CNRS UMR 7104, Inserm UMR-S 1258, 1 rue Laurent Fries, F-67400 Illkirch, France.*

[g] *CIBSS – Centre for Integrative Biological Signalling Studies, University of Freiburg, Germany*

ABSTRACT:

The NAD^+-dependent lysine deacylase Sirtuin2 (Sirt2) is involved in multiple pathological conditions, including cancer and targeting Sirt2 has thus received an increased interest for therapeutic purpose. Furthermore, addressing the ortholog from *Schistosoma mansoni* (*Sm*Sirt2) has been considered for the potential treatment of the neglected tropical disease schistosomiasis. We previously identified a 1,2,4-oxadiazole-based scaffold from the screening of the "Kinetobox" library as a dual inhibitor of human Sirt2 and *Sm*Sirt2. Herein, we describe structure-activity studies on 1,2,4-oxadiazole based analogs, which are potent inhibitors of human Sirt2 deacetylation. As proposed by docking studies, a substrate competitive and co-factor non-competitive binding mode of inhibition could be determined *in vitro* via binding assays and kinetic analysis, and further confirmed by a crystal structure of an oxadiazole inhibitor in complex with hSirt2. Optimized analogs reduced cell viability and inhibited prostate cancer cell migration, in correlation with Sirt2 deacetylase inhibition both *in vitro* and in cells.

KEYWORDS:

Sirtuin2; 1,2,4-oxadiazole; inhibitors; kinetics

INTRODUCTION:

Sirtuins (Sirts) refer to class III of Histone deacetylases (HDACs) and exert their catalytic activity in presence of nicotinamide adenine dinucleotide (NAD^+) as cofactor.[1,2] Seven isotypes are identified in humans, which share structural similarities around the catalytic core, composed by a Zn^{2+}-binding domain without catalytic role but responsible for structural stability and a so called "Rossmann"-like domain for the NAD^+ cofactor binding[3,4]. On the other hand, Sirtuins differ in their cellular localization[5–8] and catalytic activity which is displayed on a wide spectrum of histone

and non-histone proteins.[9–17] Sirtuin 2 (Sirt2) is mainly localized in the cytosol but it can also shuttle into the nucleus.[18] Together with Sirtuin 1 (Sirt1) and Sirtuin 3 (Sirt3), it has been long considered a strong deacetylase of both histone[19–21], and non-histone[22–27] substrates. Besides its well-known deacetylase activity, Sirt2 mediates also defatty-acylation with a greater catalytic efficiency[28–32], arising from a higher target affinity due to additional interactions between the acyl chain and the hydrophobic region beyond the "extended C-site" ("EC-site") of Sirt2[28,29]. A number of endogenous substrates have been also reported for Sirt2 defatty-acylation[33–35] , which prompted researchers in the field to explore further the physiological role of this activity and the potential of its inhibition. Thioacyl-lysine[36,37], thioamide and thiourea[38] mechanism-based inhibitors , as well as the triazole-SirReal-derivative **Mz242** and morpholine-SirReal-derivative (**MorSirReal**) inhibitor[39] (**Figure 1)** have been recently reported to block simultaneously Sirt2 mediated deacetylation and defatty-acylation**.** Addressing both activities appeared generally beneficial for anticancer effects compared to a selective Sirt2 deacetylase inhibition.[32,36]. However, the isotype selectivity can be lost resulting in higher cytotoxicity, which arises presumably from multiple targets or off-target action.[40] By exerting its deacetylase and defatty-acylase activity on multiple endogenous substrates, Sirt2 is associated with several diseases including cancer[41–44]. As a promoter or suppressor of multiple competing mechanisms, Sirt2 plays a controversial role, which requires further investigations[44,45] and whose inhibition may be promising for therapeutic purpose.

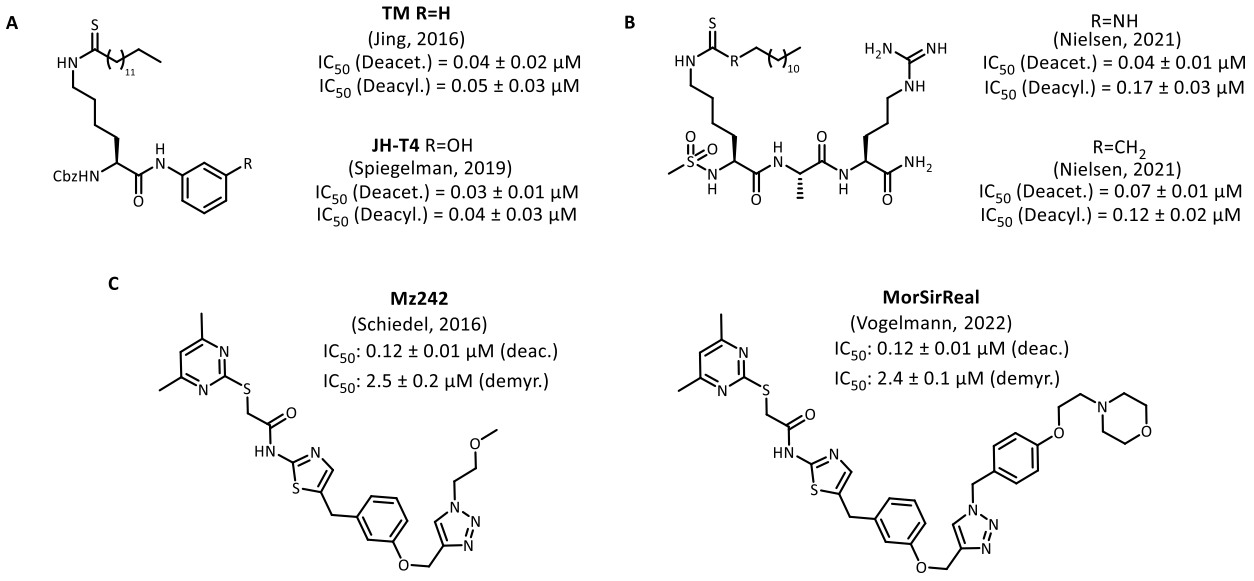

Figure 1. (A) Simultaneous inhibitors of hSirt2-mediated deacetylation and defatty-acylation **TM**[46] and its analog **JH-T4**[47]; (B) Thiourea and thioamide-based peptides[48]; (C) **Mz242** and its derivative **MorSirReal**[39].

As reported already for other regulators of the epigenetic mechanisms underlying the morphological changes during the life-cycle of parasites[49–52], Sirtuins play also a crucial role in the survival of parasites like *Schistosoma mansoni*.[53] Addressing these enzymes has been thus considered as a promising approach for the potential treatment of parasitic diseases, including schistosomiasis.[54,55] Considering the similar behavior of cancer cells and parasitic organisms, in terms of invisibility to the immune host system and metabolic activity[56–60], a "target-repurposing approach"[61,62] was successfully applied for the identification of lead compounds against parasitic epigenetic targets like *Sm*HDAC8, confirming also the importance of epigenetic regulators for the survival of the parasite.[63–66]. Five isotypes of Sirtuins are expressed in *Schistosoma mansoni* (*Sm*Sirts), and according to phylogenetic analysis they are orthologs of mammalian Sirt1, Sirt2, Sirt5, Sirt6, Sirt7.[53] Among them, Sirtuin 2 (*Sm*Sirt2) showed the highest and most homogeneous

transcript pattern throughout all life-cycle stages of the parasite[67] and further characterization *in vitro* revealed *Sm*Sirt2 as deacetylases and demyristoylases[68]. We had screened the "Kinetobox library"[69], which comprises of around 600 molecules, active against the kinetoplastids *Trypanosoma cruzi*, *Trypanosoma brucei* and *Leishmania donovani* for the potential treatment of chagas disease, sleeping sickness and leishmaniasis respectively, against *Sm*Sirt2 deacetylation. Three hits were identified for further development of potential antiparasitic inhibitors, including the N-(4-(5-((1-(3-fluoro-2-methylbenzyl)piperidin-3-yl)methyl)-1,2,4-oxadiazol-3-yl) phenyl) acetamide TCMDC-143362.[68] The latter appeared not only as a good inhibitor of *Sm*Sirt2 (IC_{50} = 14.0 ± 2.0 μM), but an even more potent scaffold for inhibition of the mammalian ortholog Sirt2 (IC_{50} = 3.6 ± 1.0 μM), representing a promising starting point also for the development of more potent Sirt2 inhibitors with potential anticancer activity. Inspired by the reported hydrophobic cavity revealed beyond the "EC-site" of Sirt2,[29] initial modifications of the scaffold had concerned the elongation of the acetamide to octanoyl and decanoyl fatty-acyl group, aiming for the inhibition of the human target as well as potentially *Sm*Sirt2, due to the putative presence of a similar hydrophobic pocket beyond the active site[29]. Nevertheless when tested *in vitro*, both derivatives lost the inhibitory activity against Sirt2 and *Sm*Sirt2.[68] Here we present potent inhibitors of Sirt2 deacetylation from structure-activity studies on the 1,2,4-oxadiazole TCMDC143362, including also the optimization of the synthetic path. Further investigations *in vitro* provided insights on the mechanism of Sirt2 inhibition by the scaffold, as evinced also by a crystal structure of the most potent compound. The inhibition of Sirt2 deacetylation by optimized analogs, observed both *in vitro* and in cells, has been correlated with reduced cell viability and block of prostate cancer cell migration. Such a readily achievable scaffold may thus serve as a

structural base for the development of additional tools, to further explore and better elucidate the promising but unclarified role of Sirt2 and its inhibition.

RESULTS AND DISCUSSION

Computational Docking and design of the study

To rationalize the interaction of the initial hit with Sirt2 we carried out docking studies using the available Sirt2 crystal structure[70] as well as the generated homology model of *Sm*Sirt2 (see Methods section for details). According to molecular docking experiments, the 2-methyl-3-fluoro-benzyl moiety of TCMDC-143362 (*R*- and *S*-isomer) interacts with the hydrophobic extended C-pocket at the back of the active site, the so-called "selectivity pocket", while the acetyl group points towards the lysine channel (**Figure 2**). Similar docking poses were obtained for the *R*- and *S*-isomer. To visualize the interaction with *Sm*Sirt2 we used a previously generated homology model of *Sm*Sirt2 and docked both isomers of TCMDC-143362 into this model structure.[71] A similar interaction was observed as in case for the human Sirt2 including the interaction of the 2-methyl 3 fluoro-benzyl moiety in the hydrophobic pocket as well as the hydrogen bond to the conserved valine (Val194).

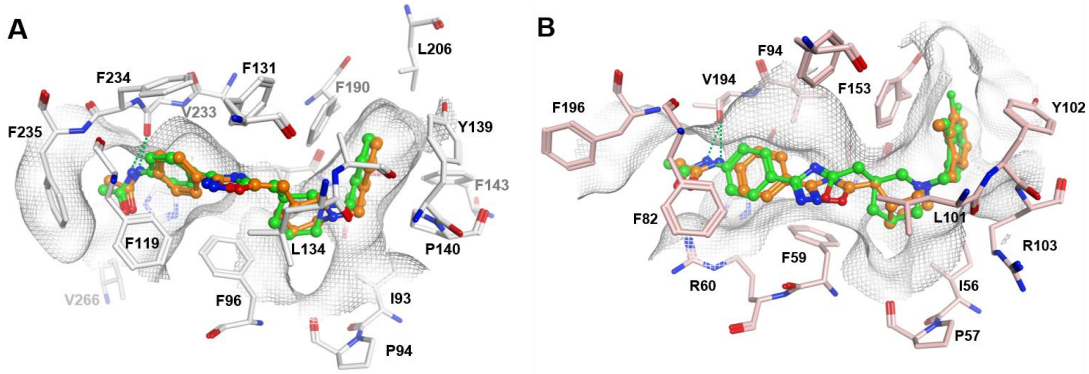

Figure 2. Predicted binding mode of TCMDC-143362 to Sirt2 (PDB ID 5DY5[70]) (A) and *Sm*Sirt2[71] (B). The ligand TCMDC-143362 and relevant binding pocket amino acid residues (or their side chains for clarity) are shown in stick representation: A) *R*-isomer (orange carbons) and *S*-isomer (green carbons) of TCMDC-143362 in hSirt2 (white carbons), B) TCMDC-143362 in *Sm*Sirt2 (pink carbons). Hydrogen bonds are depicted as green lines. Heteroatoms are colored in standard coloring scheme (nitrogen - blue, oxygen - red, fluorine - green). Binding pocket surface surrounding the ligands is shown in gray lines.

We thus designed a focussed set of TCMDC-143362 analogs which based on our predictions would have an increased potency against the desired targets. We kept the 4-(5-((1-(3-fluoro-2-methylbenzyl)piperidin-3-yl)methyl)-1,2,4-oxadiazol-3-yl)aniline core, which fits well to the selectivity pocket, but modified the acyl group pointing out of the lysine channel. Docking studies showed that the substitution of the amide linker with similar urea and thiourea linkers should be well tolerated. Furthermore, it was suggested that the replacement of the acetyl group with bigger and rigid aromatic groups is presumably beneficial for the binding due to stabilization of the bioactive conformation and potential additional hydrophobic interactions with residues at the entrance of the lysine channel. Based on the predicted binding modes we selected and synthesized a collection of compounds which can be divided in three main categories, according to the nature of the linker: the thiourea-based compounds **7** and **8**, the urea-based analogs **9**-**11** and the amides **12**-**17** (**Figure 3**).

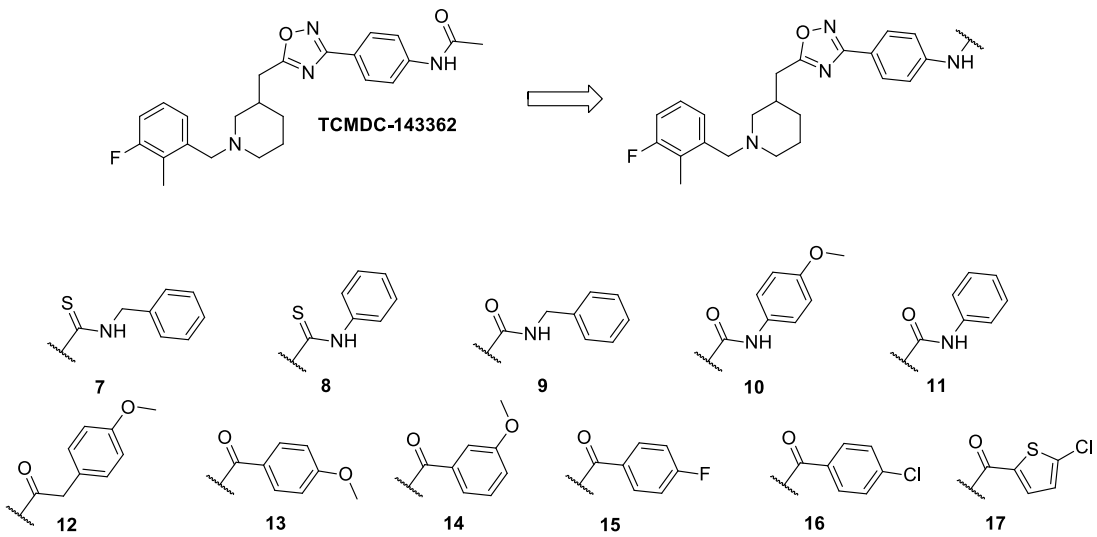

Figure 3. TCMDC-143362 and designed analogs **7-17**.

Chemical Synthesis

To obtain the desired compounds, we firstly synthesized a 1,2,4 oxadiazole-based aniline core. As illustrated in **Scheme 1,** the nucleophilic substitution of 1-(bromomethyl)-3-fluoro-2-methylbenzene **1** with ethyl 2-(piperidin-3-yl)acetate **2** provided an excellent yield of the ethyl-2-(1-(3-fluoro-2-methylbenzyl)piperidin-3-yl)acetate **3**, following the already published procedure from Monaldi et al.[68], while (Z)-tert-butyl(4-(N'-hydroxycarbamimidoyl)phenyl)carbamate **5** was obtained in good yield from the corresponding tert-butyl(4-cyanophenyl)carbamate **4** reacting with hydroxylamine hydrochloride. The coupling of (Z)-tert-butyl(4-(N'-hydroxycarbamimidoyl)phenyl)carbamate **5** with ethyl-2-(1-(3-fluoro-2-methylbenzyl)piperidin-3-yl)acetate **3** via an optimized procedure inspired by Baykov *et al.*[72], led to the formation of the 1,2,4-oxadiazole ring intermediate. Subsequent treatment with TFA in CH_2Cl_2 to remove the Boc protection afforded the final aniline core **6.**

Scheme 1. Synthesis of the aniline core intermediate **6**.

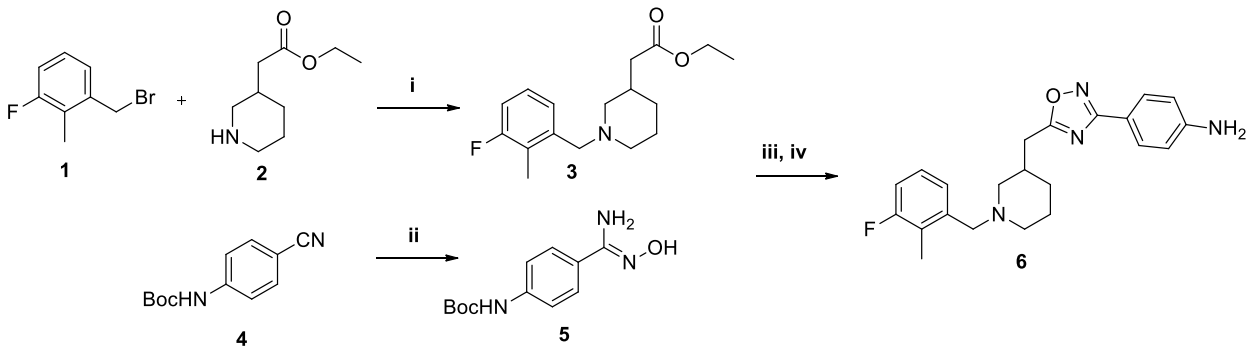

Reagents and conditions. (i) Toluene, room temperature, overnight. (ii) $NH_2OH{\cdot}HCl$, $NaHCO_3$, EtOH, reflux 6 h. (iii) NaOH, DMSO, room temperature, 4h. (iv) THF, 2h, 0-25 ° C.

Afterwards, the common intermediate **6** reacted with selected commercially available reagents to yield the desired final compounds. Thioureas **7** and **8** were obtained by coupling the aniline core with benzyl or phenyl isothiocyanate in tBuOH at reflux temperature. The reaction of the aniline core with corresponding isocyanates via urea bond formation led to compounds **9, 10,** and **11**. The acyl substitution of specific acyl chlorides with the aniline core in DCM at room temperature resulted in the formation of the amides **12-17**, all as racemates (**Scheme 2**).

Scheme 2. Synthesis of final compounds **7-17**

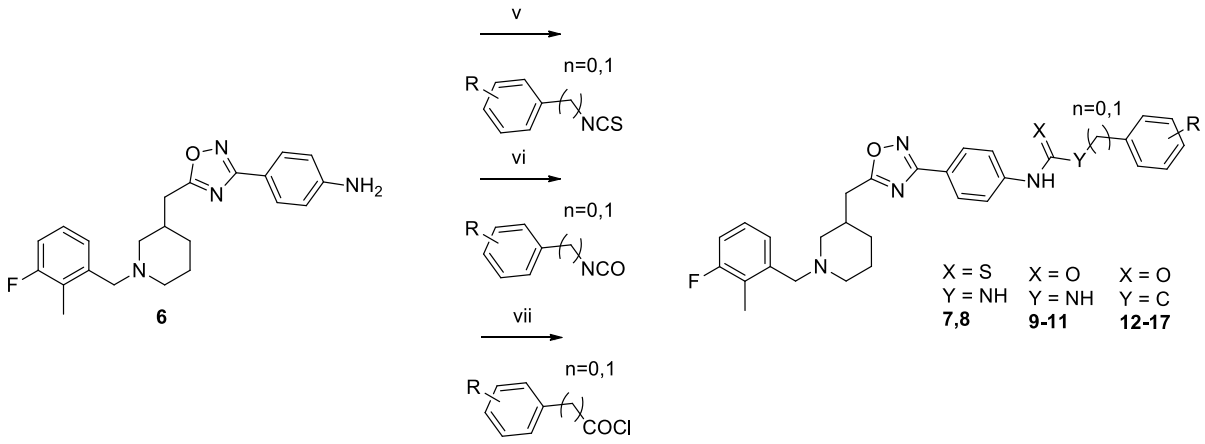

Reagents and conditions: (v) Isothiocyanate, tBuOH, reflux, 4 h. (vi) Isocyanate, DCM, room temperature, 4h. (vii) Acyl chloride, Na_2CO_3 aq. DCM, room temperature, 4h.

Biochemical *in vitro* Assays

The synthesized analogs **7-17** including the intermediate **6** were tested *in vitro* to evaluate their potential inhibitory activity against both Sirt2 deacetylation and demyristoylation as well as against *Sm*Sirt2 deacetylation and demyristoylation. Moreover, we tested our compounds against the homologous deacetylases Sirt1 and Sirt3 to investigate the isotype selectivity. For this purpose, we used an end-point homogeneous fluorescence based assay previously established in our group, where assay conditions have been adapted for specific catalytic activities as well as for the enzyme (*Sm*Sirt2 or Sirt1-3) under investigation.[68,71,73] The results are reported in **Table 1**. All compounds (except for the intermediate compound **6**) showed indeed enhanced potency against the human ortholog Sirt2, concerning Sirt2 deacetylation. We determined IC_{50} values in the very low micromolar range for compounds **8, 9, 12** and in the submicromolar range for the others, for instance compounds **11** (IC_{50}: 0.21 ± 0.02 μM) and **16** (IC_{50}: 0.35 ± 0.02 μM). The aniline intermediate **6** appeared as a 20 to 80-fold weaker inhibitor, compared to the other analogs (IC_{50}: 17.8 ± 1.37 μM).

The inhibition of Sirt2 demyristoylation observed for TCMDC-143362 (IC_{50} value 11 μM) has been mostly preserved in its synthesized analogs in a similar range (IC_{50} values between 6-28 μM) except for compounds **15-17** (less than 20% inhibition at 25 μM). A weaker potency was generally observed against Sirt2 demyristoylation (IC_{50} values between 6-28 μM), as compared to the corresponding data for Sirt2 deacetylation (IC_{50} values between 0.2-1 μM). This has been generally reported for simultaneous inhibitors, in line with the higher Sirt2 affinity displayed by

myristoylated substrates than the acetylated ones. Compared to the urea-based analogs, the thiourea **7** and **8** appeared the most potent Sirt2 demyristoylase inhibitors (IC_{50} < 10 μM). The isosteric substitution of the oxygen with a sulfur atom may thus be beneficial for this activity. In the case of amides **15-17,** no inhibition of Sirt2 demyristoylation was observed (< 15% inhibition at 25 μM). These compounds are characterized by the presence of halogen atoms in the structure, thus, these may have a negative impact on this specific activity.

All analogs generally lost potency against the parasitic target *Sm*Sirt2, as compared to the reference lead compound TCMDC-143362. Inhibition of less than 40% at 25 μM tested concentration was determined for most of the compounds. Since it was not reported in the previous work, we tested TCMDC-143362 and all new derivatives against *Sm*Sirt2 demyristoylation. In this case, a weaker potency compared to *Sm*Sirt2 deacetylation was observed for all tested molecules, including the lead compound, with percentages of inhibition mostly less than 30% at 25 μM.

When tested against the isotypes Sirt1 and Sirt3, all analogs appeared generally less active (inhibition less than 40% at 25 μM except compound **17** with 51% inhibition at 25 μM) than against Sirt2 with at least 50-fold selectivity towards Sirt2. The best selectivity was observed for the *p*-halogen substituted benzamides **15** and **16** (IC_{50} in the submicromolar range against hSirt2 and < 15% inhibition at 25 μM for both Sirt1 and Sirt3) (**Table S1** in the Supporting information).

Due to the presence of a stereocenter at position C-3 of the piperidine ring, we decided to investigate further its role in the inhibitory activity of the scaffold. We were able to separate the two enantiomers of compound **15** via preparative chiral chromatography in normal phase conditions, which were subsequently characterized via circular dichroism (see **Figure S1A and S1B** in the Supporting information). Then, we tested *in vitro* the two enantiomers in reference to

the racemate for Sirt2 deacetylation, as main activity exerted by the analog. Interestingly, both enantiomers appeared to be similarly potent as the racemate with IC_{50} values in the submicromolar range (**Table 1**).

Table 1. *In vitro* testing of TCMDC-143362, the intermediate **6** and synthesized analogs **7-17**

Sample	Sirt2 deac	Sirt2 demyr	*Sm*Sirt2 deac	*Sm*Sirt2 demyr
TCMDC-143362	3.6 ± 1.0	11.0 ± 1.20	14.0 ± 2.0	26%
6	17.8 ± 1.37	22.2 ± 1.83	30%	31%
7	0.64 ± 0.13	6.65 ± 1.01	39%	37%
8	0.90 ± 0.13	6.20 ± 1.21	< 15%	< 15%
9	1.07 ± 0.22	10.2 ± 0.45	19%	22%
10	0.62 ± 0.11	25.0 ± 1.14	33%	35%
11	0.21 ± 0.02	20.1 ± 1.57	28%	35%
12	1.10 ± 0.20	27.7 ±1.32	18%	17%
13	0.43 ± 0.04	12.6 ± 1.64	53%	21%
14	0.88 ± 0.07	22.3 ± 0.94	35%	19.0%
15	0.60 ± 0.06 rac. 0.71 ± 0.04 e1	< 15%	40%	< 15%

	0.68 ± 0.01 e2			
16	0.35 ± 0.02	18 %	40%	17%
17	0.67 ± 1.18	< 15%	35%	16%

IC_{50} values (mean ± standard deviation(SD), N ≥2) or percentage of inhibition at a concentration of 25 μM.

Structural Biology

For validation of the binding mode proposed from molecular docking, co-crystallization experiments were carried out. The crystal structure of human Sirt2 in complex with the most isotype selective inhibitor **16** was solved at 1.65 Å resolution (PDB 8PY3, **Figure 4**, **Table S2**). The complex crystallized in space group $P2_1$ with one monomer in the asymmetric unit. For co-crystallization a racemic mixture of **16** was used. Although the *in vitro* affinities of the (*S*)- and (*R*)-enantiomers were almost identical (see **Table 1**, ligand **15**), only the (*S*)-enantiomer was implemented in the final structure as it displayed a more pronounced and reliable electron density at the piperidine residue. **16** binds inside the acyl lysine channel of Sirt2 that is located at the interface of the NAD^+-binding Rossmann fold domain and the smaller, flexible Zn^{2+}-binding domain.

Superimposition of the Sirt2-**16** complex with structures containing either the cofactor NAD^+ (PDB 4RMG, **Figure S2A**)[74] or an H3-Lys-Ac substrate (PDB 4RMH, see **Figure S3A**)[74] indicate that **16** is a non-competitive inhibitor towards the co-factor NAD^+, but substrate competitive due to expected collision with the 4-chlorophenyl moiety binding next to the acyl lysine channel entry. Compound **16** opens the hydrophobic selectivity pocket of Sirt2 through its 2-methyl-3-

fluorobenzyl residue, analogous to the 4,6-dimethylpyrimidine residue of SirReal-like inhibitors. The amino acids Tyr139, Pro140, Phe143, Phe190 and Leu206 involved in the formation of this binding pocket are arranged similarly for **16** and SirReal binding. The orientation of Phe190 allows staggered π-π-stacking interactions with the 2-methyl-3-fluorobenzyl of **16**. Differently from SirReal2 and a **Mz315** bound structure, Phe96, Arg97 and Phe119 adopt here a different orientation, which explains the significantly different binding mode of **16** within the acyl lysine channel (**Figure S2A**).[70,74] The two aromatic rings of the rigid 3-phenyl-1,2,4-oxadiazole moiety are aligned almost parallel to each other, which allows partial staggered π-π-stacking with Phe119. Close to the acyl lysine channel entry N–H of the 4-chlorobenzamide residue forms a hydrogen bond of 2.9 Å distance with the main chain C=O of conserved Val233 and likely plays a crucial role in the high binding affinity of **16**. For comparison, the N_{ε}–H of peptides containing acylated lysines form analogous hydrogen bonds with Val233 in the Sirt2 bound form which is considered as one of the key interactions in substrate binding.[29,74] Compared to the intermediate **6**, the main affinity boost of **16** is realized through the implementation of the 4-chlorophenyl residue that exhibits possible weak π-π-stacking and non-specific hydrophobic interactions with Phe235 and Leu239.

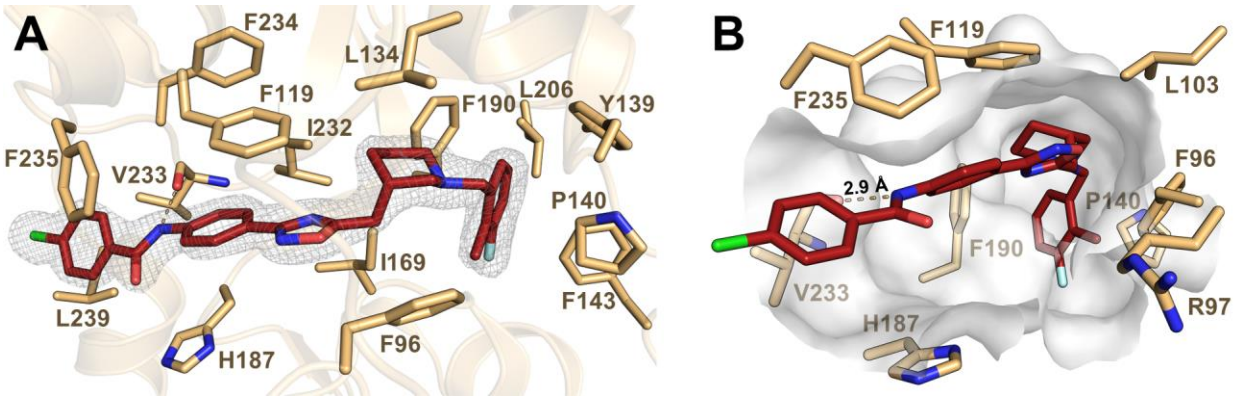

Figure 4. Co-crystal structure of the Sirt2-**16** complex. (A) Binding mode of **16** inside the acyl lysine channel of Sirt2 (light orange cartoon and sticks). **16** is shown as firebrick sticks (nitrogen = blue, oxygen = red, fluorine = light teal, chlorine = green). The $2F_o - F_c$ map is depicted as gray mesh and contoured at 1.0σ. The hydrogen bond between the amide carbonyl of V233 and the amide NH of the inhibitor is shown as dashed line. (B) Visualization of **16** binding inside the acyl lysine channel of Sirt2. The 4-chlorobenzamide residue is located at the channel entry where usually acylated lysine substrate binding takes place.

Computational docking

A slightly different geometry was observed between the docking pose of **16** in complex with Sirt2 using the structure 5DY5 and the determined crystal structure, implying a conformational change of Phe96 and Phe119 (**Figure S4**). Compared to the SirReal bound Sirt2 structure (5DY5), Phe96 is in fact rotated 180° in the **16**-bound structure (8PY3). Redocking of **16** using structure Sirt2-16 (8PY3) resulted in high agreement with the experimentally observed inhibitor binding (RMSD heavy atoms 0.30 Å, **Figure S5**).

To explain the activity of optimized compounds towards Sirt2, we docked them to the human target, using the obtained crystal structure (8PY3). The binding modes of all analogs to Sirt2 were similar (exemplified by compound **16** in **Figure S5**) and resulted in high agreement with the experimental observations of the cocrystal structure of compound **16** (**Figure 4)**. According to structure-activity relationship, the main gain in target affinity and potency seems to arise from the introduction of the aromatic ring, as the result of additional π or hydrophobic interactions of the ligand with aliphatic and aromatic side chain at the entrance of the active site, while the nature of the linker may not play a crucial role.

Docking of TCMDC-143362 to *Sm*Sirt2-HM (**Figure 2B**) suggested that a similar binding mode of synthesized analogs to the parasitic enzyme would have been possible. However, the different

amino acid residue constitution of the selectivity pocket in *Sm*Sirt2 compared to human Sirt2 (Ala106/Phe143, Arg203/Pro140, Glu168/Leu206) might be the main reason of the strongly reduced activity of the compounds on *Sm*Sirt2. The suggested binding mode could not be obtained in Sirt1 and Sirt3, since the Sirt2-specific protein conformation, needed to accommodate the ligand in the proposed orientation, could not be observed for the other isotypes.

In vitro **binding investigations**

Thermal Shift Assay

We then proceeded by testing our compounds via differential scanning fluorimetry (DSF), also referred to as Thermal Shift Assay (TSA).[74] As positive control we included **SirReal2**, which is reported as a potent Sirt2 deacetylase inhibitor *in vitro* and induced protein stabilization upon binding.[74] Compounds were tested at 5 and 25 µM with Sirt2-apoenzyme or with Sirt2 in presence of NAD^+. As illustrated for the representative cases **6**, **16** at 25 µM in presence of NAD^+ (**Figure 5**, detailed measurements are reported in **Table S3** of the Supporting Information), 1,2,4-oxadiazole-based derivatives induced generally a protein stabilization upon binding to Sirt2, resulting in a positive shift of the melting temperature in presence of the ligand compared to the DMSO control (reference used for no ligand binding). Compound **6** did not exhibit stabilizing effect compared to the DMSO control (no significant thermal shift observed), which can be correlated with its low potency as Sirt2 inhibitor *in vitro*.

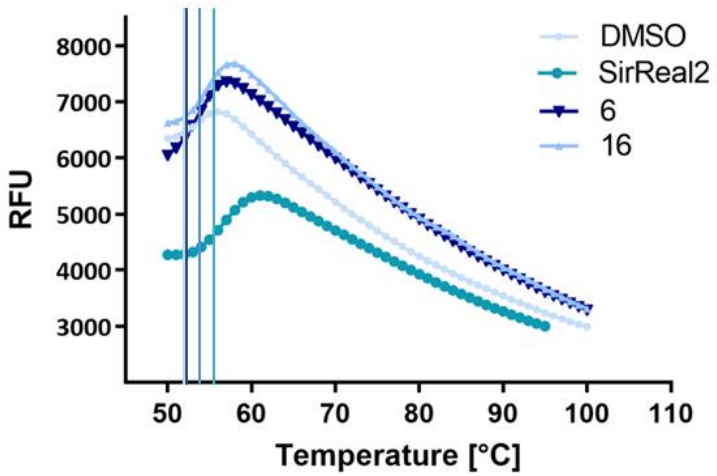

Figure 5. Thermal stability plots of Sirt2-NAD$^+$ complex (DMSO) and in presence of the analogs **6, 16** and **SirReal2** as positive control.

Fluorescence Polarization assay

Furthermore, a fluorescence polarization (FP) binding assay was previously established in our group[75] which allows the evaluation of ligand binding specifically to the "selectivity" pocket of Sirt2. In competition with a TAMRA SirReal-based derivative used as probe, we tested exemplary compounds of the series **6**, **7**, **11**, **16** and **SirReal2** at 25, 5 and 1 μM. As illustrated in **Figure 6,** all compounds displaced the fluorescent probe in a dose-dependent manner and consistently with their potency as Sirt2 inhibitors observed in the homogeneous fluorescence-based assay. According to the co-crystal structure of **16** (**Figure 4**), the aniline core **6** also binds to the selectivity pocket through the conserved 2-methyl3-fluorobenzyl moiety and is able to displace the probe at high concentration. The most potent compounds **11** and **16** exhibited more than 50% inhibition of probe binding at low concentration, similarly to **SirReal2**, whereas the inhibitor **7** displayed a weaker probe displacement.

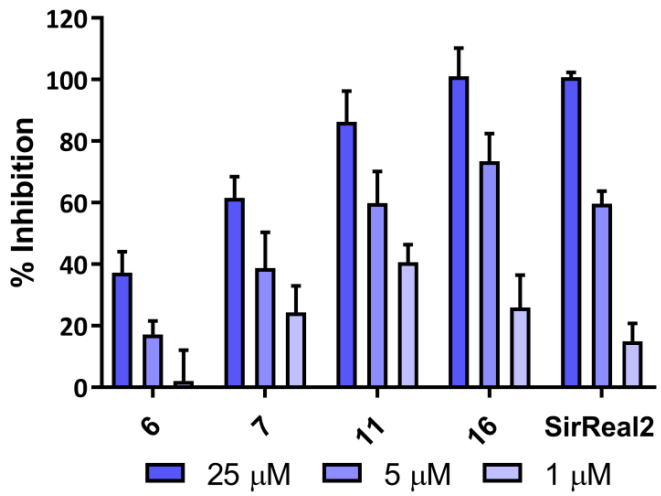

Figure 6. Inhibition (%) of fluorescent probe binding to the selectivity pocket by analogs **6**, **7, 11, 16** and **SirReal2** at 25, 5 and 1 μM. Values are presented as mean ± SD (N≥2).

Kinetic analysis

Recently we established a continuous set-up[39] of the homogeneous fluorescence-based assay, which prompted us to conduct kinetic analysis of representative compounds **7**, **9**, **11**, **16** to explore further the mechanism of binding and inhibition of our scaffold. A linear trend of the enzymatic progress curves was observed over time with decreasing rate at higher inhibitor concentration, which suggested a fast-on/fast-off steady-state binding mode for our compounds (plots can be found in **Figure S6** of the Supporting Information). Then, we investigated the modality of inhibition for exemplary compounds, performing competition analysis against the substrate (ZMAL) and the cofactor (NAD^+). By determining an increase of the apparent Michaelis-Menten constant values (K_M) and a general conservation of the maximum velocity (v_{max}) at higher inhibitor concentration, we assigned a substrate-competitive binding mode (**Figure 7A** for compound **16**, other analogs can be found in the Supporting Information **Figure S7**). On the other hand, considering the decrease of maximum velocity by raising the ligand concentration, our compounds

appeared partial non-competitive inhibitors towards the cofactor NAD^+ (**Figure 7B** for compound **16**, other analogs can be found in the Supporting Information **Figure S8**). This result is consistent with the structural investigations (for **16**) and in general docking studies, where the ligand protrudes towards the lysine channel without interfering with the NAD^+ binding site.

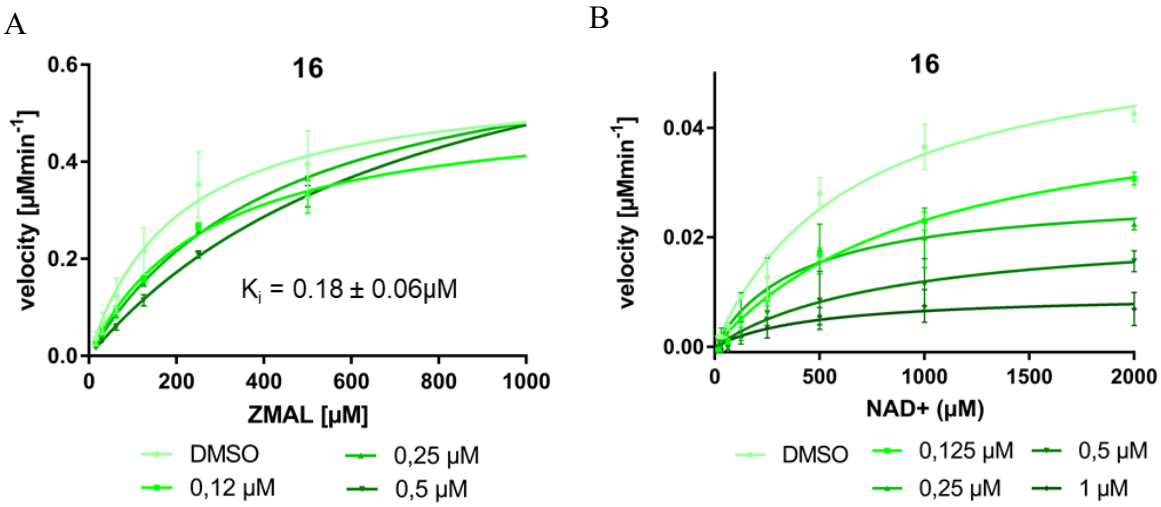

Figure 7. (A) Michaelis-Menten plots of Sirt2 and determination of kinetic parameters K_M and v_{max} at various concentrations of compound **16**, revealing a substrate competitive and (B) a cofactor non-competitive binding inhibition. Values reported as mean ± SD.

Cellular investigations

α-tubulin hyperacetylation

Afterwards, we investigated the potential inhibition of Sirt2 deacetylation in a cellular environment. α-tubulin is a well-known substrate of Sirt2 deacetylation[76] and the variation on the α-tubulin acetylation level can be used as an indirect readout for the cellular target engagement of Sirt2 deacetylase inhibitors. Metastatic prostate cancer (PC3MLuc) cells were treated with compounds **6**, **7**, **15**, **16** and **MorSirReal** as positive control[39] at 20 µM for 6 hours before

immunostaining and readout via immunofluorescence microscopy. In agreement with their potency observed *in vitro* as Sirt2 deacetylase inhibitors, α-tubulin acetylation levels for the submicromolar range inhibitors **7**, **15** and **16** were higher compared to the weak inhibitor **6,** suggesting the cellular inhibition of Sirt2 mediated deacetylation by the oxadiazoles. The positive control **MorSirReal** induced a more significant hyperacetylation of α-tubulin in respect to compounds **7**, **15** and **16**, which is also consistent with its higher potency *in vitro* and apparent better solubility (**Figure 8** shows the DMSO control, the positive control **MorSirReal** and the inhibitors **6**,**7** and **16**, detailed data can be found in the Supporting Information, **Figure S9**).

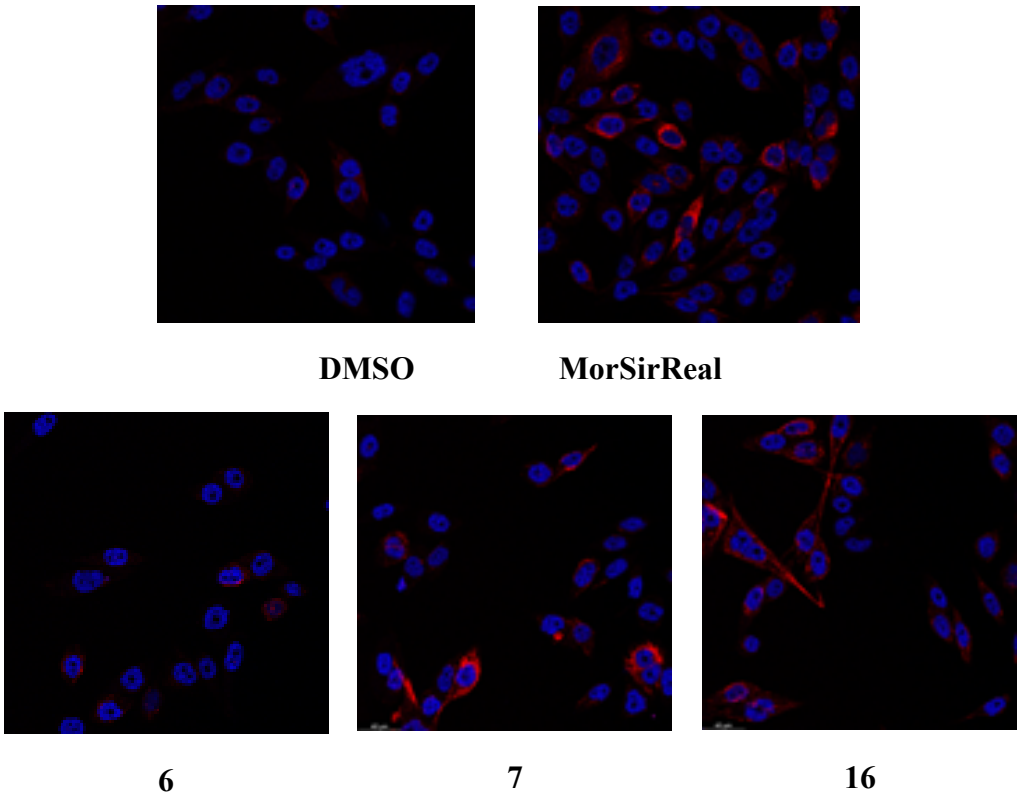

Figure 8. α-tubulin acetylation levels by immunofluorescence microscopy. PC-3M-luc cells were treated with Sirt2 inhibitors **6**, **7**, **16**, **MorSirReal**[31] or DMSO at 20 μM for 6 hours before imaging. (n = 3) The images show acetylation levels of α-tubulin in red and the DAPI-stained nuclei in blue.

MTS assay

We then investigated effects on cell viability, treating Hela cells with a selection of compounds (inhibitors **6**, **7** and **16**) at 25, 5 and 1 µM via MTS assay for 3 days at 37 °C (**Figure 9A**). In agreement with their potency against Sirt2 deacetylation *in vitro*, inhibitors **7** and **16** reduced cell viability in a dose dependent manner, whereas the weaker compound **6** showed only weak or no effects.

Migration assay

Lastly, metastatic prostate cancer (PC3MLuc) cells were treated with the inhibitor **16** and the negative control **6**, together with **MorSirReal** as positive control[39], at 20 and 10 µM for 3 days at 37 °C, to investigate the effects of selected 1,2,4-oxadiazole hSirt2 inhibitors on cancer cell migration . Compound **16** inhibited cell migration in a similar manner to the positive control **MorSirReal**, while the weak inhibitor **6** did not show significant effects (**Figure 9B**). Thus, we conclude a correlation between the effects on cancer cell migration and the Sirt2 inhibition by 1,2,4-oxadiazoles.

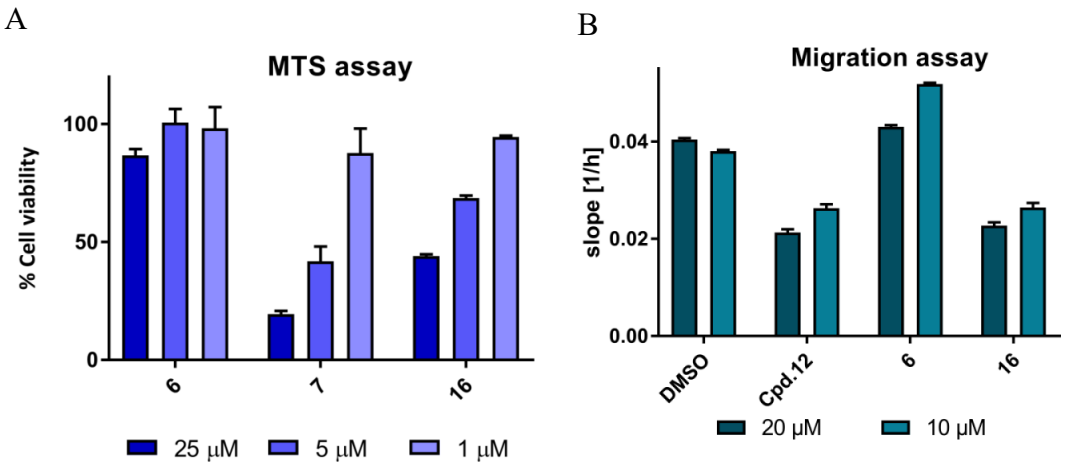

Figure 9. (A) Effects on viability (%) of Hela cells by selected analogs **6**, **7**, **16**, tested at 25, 5 and 1 µM via MTS assay with an incubation time of 3 days. Values reported as mean ± SD. (B) Cell migration (%) after treatment of PC3MLuc cells with compounds **6**, **16** and **MorSirReal**[31] at 20 and 10 µM. Values reported as mean ± SD.

CONCLUSIONS:

Based on docking studies of a previously identified 1,2,4-oxadiazole scaffold TCMDC-143362 to both human and *Schistosoma mansoni* Sirt2, a focused set of analogs was designed to potentially increase their target affinity and its inhibition. Inspired by the revisited "amidoxime route"[72], derivatives were synthesized and afterwards evaluated *in vitro* via homogeneous fluorescence-based assays.[71,73] Regardless the stereochemistry, all analogs are potent inhibitors of human Sirt2-mediated deacetylation *in vitro* with IC_{50} values in the very low or submicromolar range and a promising activity also against demyristoylation. The crystal structure of Sirt2 in complex with the most potent compound **16** elucidated the binding mode of the scaffold, characterized by a substrate competitive and NAD^+ partially non-competitive mechanism of inhibition, as confirmed also via additional *in vitro* investigations. By inhibiting Sirt2 deacetylation also in cells, selected compounds reduced cell viability and inhibited cancer cell migration. The optimization of TCMDC-143362 led to a readily achievable potent scaffold against Sirt2

deacetylation, which contributes to expand the spectrum of small molecules targeting Sirt2 for therapeutic application, and to the design of additional tools, e.g. Proteolysis targeting chimeras (PROTACs) to further explore the role of this protein in cancer but also other diseases.

EXPERIMENTAL SECTION

General chemistry conditions. Reagents, starting materials and solvents were used without further purification of purchased forms. All reactions were monitored by Thin-layer chromatography (TLC) with Merck pre-coated silica gel 60 F_{254} plates and analyzed under UV light (254 nm). All compounds were purified via flash column chromatography, using a Biotage Isolera Prime/One system, applying specific gradients on 40–60 µm pre-packed silica gel columns from Biotage®, HP-spherical 50 µm pre-packed silica gel columns from Interchim (Jumbo Pack), Sfär Silica D 60 mm, Sfär KP amino D 50 mm or Sfär Silica HC D 20 µm pre-packed silica gel columns from Biotage®. The purity of all tested compounds was determined by HPLC, with an Agilent Technologies 1260 Infinity II system using diode array detector (DAD) UV detection 210 nm, and it was equal or higher than 95 %. Following conditions were used: eluent A, water + 0.05 % TFA; eluent B, acetonitrile + 0.05 % TFA; linear gradient conditions (0-29 min, linear increase from A = 100 % and B = 0 % to A = 0 % and B = 100 %; 29-31 min, B = 100 %; 31 min, decrease to B = 10 %; 31-40 min B = 10 %) with a flowrate of 1 mL/min; analytical column: Phenomenex Kinetex 5 µm XB-C18 100 Å, 250 mm X 4.6 mm. Enantiomers of compound **15** were separated via chiral chromatography (Phenomenex Lux 5 µm Cellulose-1, 250 mm X 10 mm) using following conditions: eluent A, n-hexane; eluent B, isopropanol; linear gradient conditions (0-90 min, linear increase from A = 10 % to B = 10.5 %). Compounds were

characterized via Low Resolution Mass Spectrometry (LRMS) with an Advion expression CMS using Atmospheric Pressure Chemical Ionization (APCI) as ion source on a Thermo Scientific Exactive mass spectrometer or via High Resolution Mass Spectrometry (HRMS) using electrospray ionization (ESI) as ion source on THERMO SCIENTIFIC Advantage. Proton (^{1}H) and carbon (^{13}C) spectra were recorded on BrukerAvance III HD spectrometer at 400 MHz and 100 MHz respectively, using deuterated chloroform $CDCl_3$ or deuterated dimethyl sulfoxide DMSO-d_6. Chemical shifts δ are given in part per million (ppm) and peak assignment was supported by COSY experiments (abbreviations for multiplicities: s, singlet; d, doublet; t, triplet; q, quartet; m, multiplet). Coupling constant (J) are expressed in Hz. Peak assignments for 1H NMR were made via COSY experiments. Enantiomers of compound **15** were further characterized via circular dichroism, using a Jasco J 810 spectropolarimeter (Jasco, Pfungstadt, Germany) device, measuring the absorption and circular dichroism in a UV-vis range between 220-380 nm.

Synthesis of ethyl2-(1-(3-fluoro-2-methylbenzyl)piperidin-3-yl)acetate (**3**). Ethyl2-(1-(3-fluoro-2-methylbenzyl)piperidin-3-yl)acetate (**3**) was synthesized according to a published procedure[77]. 2-(Piperidin-3-yl)aceticacidethylester (1.1 g, 6.5 mmol) was dissolved in toluene (2.7 mL), followed by the addition of Et_3N (13.1 mmol, 1.8 mL) and 3-fluoro-2-methylbenzylbromide (1.3 g, 6.4 mmol) at 0 °C. After 10 min, the mixture was warmed up and stirred at room temperature. After 18 h, the precipitate was removed by filtration, washed with cyclohexane (Cy), and the filtrate was concentrated. The product was dried using a vacuum pump for 3 h and and then purified by flash column chromatography on SiO_2 gel with CH_2Cl_2/MeOH (9/1). Colorless oil; 1.71 g, yield 91 %. R_f = 0.60 (10 % MeOH in CH_2Cl_2). ^{1}H NMR (400 MHz, DMSO-d_6) δ [ppm]: 7.17–7.12 (m, 1H, C*H* benzyl), 7.05–7.00 (m, 2H, C*H* benzyl), 3.99 (q, ^{3}J(H,H) = 7.9 Hz, 2H, CH_2CH$_3$), 3.39 (s, 2H, CH_2 benzyl), 2.68–2.55 (m, 2H, CH_2CO$_2$), 2.20 (s, 3H, CH_3 benzyl), 2.25–

2.14 (m, 2H, $CH_2CH_2CH_2$ piperidine), 2.04–1.97 (m, 1H, NCH_2CH piperidine), 1.93–1.83 (m, 1H, C*H*, piperidine), 1.81–1.74 (m, 1H, NCH_2CH piperidine), 1.66–1.60 (m, 1H, NCH_2CH_2 piperidine), 1.60–1.53 (m, 1H, NCH_2CH_2 piperidine), 1.46–1.35 (m, 1H, $CHCH_2CH_2$ piperidine), 1.04–0.92 (m, 1H, $CHCH_2CH_2$ piperidine).^{13}C NMR (101 MHz, DMSO-d_6) δ [ppm]: 171.9 (*C*O), 160.8 (d, ^{1}J(C,F) = 243.4 Hz, *C*F benzyl), 139.5 (d, ^{3}J(C,F) = 5.6 Hz, CH_{meta} benzyl), 126.4 (d, ^{3}J(C,F) = 9.1 Hz, *C*CH_2 benzyl), 125.4 (d, ^{4}J (C,F) = 2.8 Hz CH_{para} benzyl), 123.7 (d, ^{2}J(C,F) = 16.0 Hz, CH_{ortho} benzyl), 113.5 (d, ^{2}J(C,F) = 23.3 Hz, CH_3C benzyl), 60.3 (CH_2CH_3), 59.7 (NCH_2 benzyl), 58.6 (NCH_2 piperidine), 53.6 (NCH_2 piperidine), 38.2 (CH_2CO_2), 32.8 (CH_2, piperidine), 29.9 (CH_2, piperidine), 24.4 (*C*H piperidine), 14.1 (CH_2CH_3), 10.0 (d, ^{3}J(C,F) = 6.0 Hz, CH_3). ^{19}F NMR (376 MHz, DMSO-d_6) δ [ppm]: -117.8 (m, C*F*). LRMS (APCI): m/z calcd. for $C_{17}H_{24}FNO_2$+ H^+ $[M+H]^+$ 294.3, found 294.3.

*Synthesis of tert-butyl(4-(N'-hydroxycarbamimidoyl)phenyl]carbamate (**5**).* To a stirred suspension of *tert*-butyl(4-cyanophenyl)carbamate (499.3 mg, 2.3 mmol) and $NH_2OH{\cdot}HCl$ (246.6 mg, 3.4 mmol) in EtOH (25 mL) $NaHCO_3$ (351.7 mg, 3.45 mmol) was added. The reaction mixture was stirred under reflux for 6 h. Afterwards it was concentrated under reduced pressure and the residue was diluted with cold water (10 mL). The resulting precipitate was filtered off and washed with cold water (70 mL). The crude was then purified by flash chromatography on SiO_2 gel with CH_2Cl_2/MeOH (9/1) to afford 5. White solid; 0.397 g, yield 69 %. R_f = 0.52 (10 % MeOH in CH_2Cl_2). ^{1}H NMR (400 MHz, DMSO-d_6) δ [ppm]: 9.59 (s, 1H, N*H* carbamate), 9.52 (s, 1H, O*H*), 7.55 (m(AA'BB'), 2H, C*H* phenyl), 7.43 ((m(AA'BB'), 2H, C*H* phenyl), 5.71 (s, 2H, NH_2), 1.57 (s, 9H, $C(CH_3)_3$). ^{13}C NMR (101 MHz, DMSO-d_6) δ [ppm]: 152.7 (*C* amidoxime), 150.5 (*C*O carbamate), 140.1 (*C*CNH_2 phenyl), 127.0 (2C, *C*H phenyl), 125.8 (2C, *C*H benzyl), 117.4 (*C*NH

benzyl), 79.2 (O*C*(CH_3)$_3$), 28.1 (OC(*C*H_3)$_3$). LRMS (APCI): m/z calcd. for $C_{12}H_{17}N_3O_3$ + H^+ $[M+H]^+$ 252.2, found 252.1.

Synthesis of N-tert-butyl(4-(5-((1-(3-fluoro-2-methylbenzyl)piperidin-3-yl)methyl)-1,2,4-oxadiazol-3-yl)phenyl)carbamate ***(6a)****.* To a solution of ethyl2-(1-(3-fluoro-2-methylbenzyl)piperidin-3-yl)acetate **3** (1.7 g, 5.8 mmol) and *tert*-butyl(4-(N'-hydroxycarbamimidoyl)phenyl]carbamate **5** (0.9 g, 3.9 mmol) in DMSO (3.9 mL) powdered NaOH (0.3 g, 6.3 mmol) was rapidly added. The reaction mixture was stirred at room temperature for 4 h. The reaction mixture was diluted with cold water (10 mL). The aqueous phase was extracted with Cy (5x 6 mL). The organic fractions were dried with Na_2SO_4 and concentrated under reduced pressure. The crude was then purified by flash chromatography on SiO_2 gel with CH_2Cl_2/MeOH (9/1), yielding the intermediate **6a**. Colourless oil; 0.49 g, yield 54 %. R_f = 0.65 (10 % MeOH in CH_2Cl_2). ^{1}H NMR (400 MHz, DMSO-d_6) δ [ppm]: 9.72 (s, 1H, N*H* carbamate), 7.83 ((m(AA'BB'), 2H, C*H* anilide), 7.62 ((m(AA'BB'), 2H, C*H* anilide), 7.15–6.98 (m, 3H, C*H* benzyl), 3.42 (s, 2H, CH_2 benzyl), 2.98–2.86 (m, 2H, $CH_2CH_2CH_2$ piperidine), 2.77–2.72 (m, 1H, CH_2CO), 2.60–2.55 (m, 1H, CH_2CO), 2.21 (s, 3H, CH_3 benzyl), 2.10–2.03 (m, 2H, NCH_2CH$_2$ piperidine), 1.96–1.89 (m, 1H, C*H* piperidine), 1.71–1.58 (m, 2H, NCH_2CH piperidine), 1.49 (s, 9H, C(CH_3)$_3$), 1.48–1.46 (m, 1H, CH_2CH_2CH piperidine), 1.18–1.08 (m, 1H, CH_2CH_2CH piperidine). ^{13}C NMR (101 MHz, DMSO-d_6) δ [ppm]: 178.9 (*C*O), 167.2 (O*C*N oxadiazole), 160.7 (d, ^{1}J(C,F) = 241.9 Hz, *C*F benzyl), 152.6 (N*C*N oxadiazole), 142.4 (*C*NH anilide), 139.4 (d, ^{3}J(C,F) = 4.1 Hz, *C*H$_{meta}$ benzyl), 127.7 (2C, *C*H anilide), 126.3 (d, ^{3}J(C,F) = 9.1 Hz, *C*CH$_2$ benzyl), 125.4 (d, ^{4}J(C,F) = 2.6 Hz, *C*H$_{para}$ benzyl), 123.6 (d, ^{2}J(C,F) = 15.9 Hz, *C*H$_{ortho}$ benzyl), 119.6 (*C*C anilide), 118.1 (2C, *C*H anilide), 113.6 (d, ^{2}J(C,F) = 23.1 Hz, CH_3*C* benzyl), 79.6 (*C*(CH_3)$_3$), 60.1 (NCH_2 benzyl), 58.3 (N*C*H$_2$ piperidine), 53.4 (NCH_2 piperidine), 34.1 (*C*H_2CO),

29.9 (N*C*H_2 piperidine), 29.6 (*C*H_2, piperidine), 28.1, ((*C*H_3)$_3$), 26.3 (*C*H piperidine), 10.0 (d, ^{3}J(C,F) = 5.1 Hz, *C*H_3). LRMS (APCI): m/z calcd. for $C_{27}H_{33}FN_4O_3$ + H^+ $[M+H]^+$ 481.5, found 481.1.

*Synthesis of (4-(5-((1-(3-fluoro-2-methylbenzyl)piperidin-3-yl)methyl)-1,2,4-oxadiazol-3-yl)phenyl)aniline (**6**).* To a stirred solution of N-*tert-butyl*(4-(5-((1-(3-fluoro-2-methylbenzyl)piperidin-3-yl)methyl)-1,2,4-oxadiazol-3-yl) phenyl)carbamate (0.32 g, 0.7 mmol) in CH_2Cl_2 (1.8 mL) was added trifluoroaceticacid (0.3 g, 3.1 mmol, 0.4 mL) at 0 °C and stirred for 2 h at 25 °C. After completion of the reaction the mixture was neutralized with $NaHCO_3$ saturated solution, the product was extracted with AcOEt (3x6 mL) and the organic fractions concentrated under reduced pressure. The crude was then purified by flash chromatography on SiO_2 gel with CH_2Cl_2/MeOH (9/1) to obtain **6.** Yellow oil; 0.32 g, yield 90 %. R_f = 0.48 (10 % MeOH in CH_2Cl_2). ^{1}H NMR (400 MHz, DMSO-d_6) δ [ppm]: 7.60 ((m(AA'BB'), 2H, C*H* anilide), 7.12–7.01 (m, 3H, C*H* benzyl), 6.63 ((m(AA'BB'), 2H, C*H* anilide), 5.75 (s, 2H, N*H*$_2$ aniline), 3.42 (s, 2H, C*H*$_2$ benzyl), 2.97–2.83 (m, 2H, $CH_2CH_2CH_2$ piperidine), 2.79–2.71 (m, 1H, C*H*$_2$CO), 2.67–2.56 (m, 1H, C*H*$_2$CO), 2.21 (s, 3H, C*H*$_3$ benzyl), 2.11–2.02 (m, 2H, NC*H*$_2$CH$_2$ piperidine), 1.95–1.86 (m, 1H, C*H* piperidine), 1.75–1.55 (m, 2H, NC*H*$_2$CH piperidine), 1.50–1.38 (m, 1H, CH_2CH_2CH piperidine), 1.14–1.08 (m, 1H, CH_2CH_2CH piperidine). ^{13}C NMR (101 MHz, DMSO-d_6) δ [ppm]: 167.7 (O*C*N oxadiazole), 160.7 (d, ^{1}J(C,F) = 241.4 Hz, *C*F benzyl), 151.7 (N*C*N oxadiazole), 139.4 (d, ^{3}J(C,F) = 3.1 Hz, *C*H$_{meta}$ benzyl), 128.3 (2C, *C*H anilide), 126.3 (d, ^{3}J(C,F) = 9.1 Hz, *C*CH$_2$ benzyl), 125.4 (d, ^{4}J(C,F) = 2.4 Hz, *C*H$_{para}$ benzyl), 123.7 (d, ^{2}J(C,F) = 16.2 Hz, *C*H$_{ortho}$ benzyl), 113.5 (*C*NH$_2$ anilide), 113.5 (d, ^{2}J(C,F) = 23.7 Hz, CH$_3$*C* benzyl), 113.5 (2C, *C*H anilide), 112.7 (C*C* anilide), 60.1 (N*C*H$_2$ benzyl), 58.4 (N*C*H$_2$ piperidine), 53.4 (N*C*H$_2$ piperidine), 34.1 (*C*H$_2$CO), 29.9 (*C*H$_2$, piperidine), 29.7 (*C*H$_2$, piperidine), 24.3 (*C*H,

piperidine), 10.0 (d, $^{3}J(C,F)$ = 5.1 Hz, *C*H_3). ^{19}F NMR (376 MHz, DMSO-d_6) δ [ppm]: -117.7 (m, C*F*). LRMS (APCI): m/z calcd. for $C_{22}H_{25}FN_4O$ + H^+ $[M+H]^+$ 381.4, found 381.1.

Synthesis of 1-(benzyl or phenyl)-3-(4-(5-((1-(3-fluoro-2-methylbenzyl)piperidin-3-yl)methyl)-1,2,4-oxadiazol-3-yl)phenyl)thioureas (7-8). To a solution of isothiocyanate (1.0 equiv.) in *t*-BuOH (2.2 mL), (4-(5-((1-(3-fluoro-2-methylbenzyl) piperidin-3-yl)methyl)-1,2,4-oxadiazol-3-yl)phenyl)aniline **6** (1.2 equiv.) was added. The mixture was stirred under refluxed for 4 h. The reaction mixture was concentrated under reduced pressure, then CH_2Cl_2 (10 mL) was added and the organic phase was washed with HCl (aq. 5 %, 3 × 10 mL), dried with anhydrous $Na_2SO_4$and evaporated under reduced pressure.

Synthesis of 1-benzyl-3-(4-(5-((1-(3-fluoro-2-methylbenzyl)piperidin-3-yl)methyl)-1,2,4-oxadiazol-3-yl)phenyl)thiourea (7). The crude was purified by flash chromatography on SiO_2 gel with CH_2Cl_2/MeOH (92/8) yielding **7**. White crystalline solid, 70 mg, yield 71 %. R_f =0.52 (10 % MeOH in CH_2Cl_2). ^{1}H NMR (400 MHz, DMSO-d_6) δ [ppm]: 9.95 (s, 1H, N*H* urea), 8.45 (s, 1H, N*H* urea), 7.88 ((m(AA'BB'), C*H* anilide), 7.71 ((m(AA'BB'), C*H* anilide), 7.36–7.35 (m, 4H, C*H* benzyl), 7.29–7.25 (m, 1H, C*H* benzyl), 7.15–6.98 (m, 3H, C*H* fluoro-benzyl), 4.76–4.75 (d, 2H, CH_2NH benzyl), 3.42 (s, 2H, CH_2 benzyl), 3.00–2.88 (m, 2H, $CH_2CH_2CH_2$ piperidine), 2.76–2.74 (m, 1H, CH_2CO),), 2.62–2.55 (m, 1H, CH_2CO), 2.22 (s, 3H, CH_3 benzyl), 2.09–2.05 (m, 2H, NCH_2CH_2 piperidine), 1.95–1.90 (m, 1H, C*H* piperidine), 1.72–1.59 (m, 2H, NCH_2CH piperidine), 1.49–1.41 (m, 1H, CH_2CH_2CH piperidine), 1.17–1.09 (m, 1H, CH_2CH_2CH piperidine). ^{13}C NMR (101 MHz, DMSO-d_6) δ [ppm]: 180.5 (*C*S), 179.1 (N*C*N oxadiazole) 167.1 (O*C*N oxadiazole), 160.7 (d, $^{1}J(C,F)$ = 241.3 Hz, *C*F benzyl), 142.4 (*C*NH anilide), 139.4 (d, $^{3}J(C,F)$ = 5.1 Hz, *C*H$_{meta}$ benzyl), 138.7 (*C*CH_2 benzyl), 128.3 (2C, *C*H benzyl), 127.5 (2C, *C*H anilide), 127.4 (2C, *C*H anilide), 127.0 (2C, *C*H benzyl), 126.3 (d, $^{3}J(C,F)$ = 9.1 Hz, *C*CH_2 benzyl),

125.4 (d, ^{4}J(C,F) = 3.0 Hz, *C*H$_{para}$ benzyl), 123.7 (d, ^{2}J(C,F) = 16.1 Hz, *C*H$_{ortho}$ benzyl), 122.3 (*C*C anilide), 121.1 (*C*H benzyl), 113.6 (*C*C benzyl), 113.3 (d, ^{2}J(C,F) = 23.2 Hz, CH$_3$*C* benzyl), 60.1 (N*C*H$_2$ benzyl), 58.3 (N*C*H$_2$ piperidine) 53.4 (N*C*H$_2$ piperidine), 47.1 (NH*C*H$_2$), 34.1 (CO*C*H$_2$), 29.9 (*C*H$_2$ piperidine), 29.7 (*C*H$_2$ piperidine), 24.1 (*C*H piperidine), 10.0 (d, ^{3}J(C,F) = 5.0 Hz, *C*H$_3$). HRMS (ESI): m/z calcd. for $C_{30}H_{32}FN_5OS$ + H^+ $[M+H]^+$ 530.68, found 530.24. HPLC analysis: retention time = 16.735 min; peak area, 99 %.

*Synthesis of 1-(4-(5-((1-(3-fluoro-2-methylbenzyl)piperidin-3-yl)methyl)-1,2,4-oxadiazol-3-yl) phenyl)-3-phenylthiourea (**8**).* The crude was then purified by flash chromatography on SiO_2 gel with CH_2Cl_2/MeOH (0-10 %), to afford **8**. White crystalline solid; 70 mg, yield 44 %. R_f = 0.52 (10 % MeOH in CH_2Cl_2). ^{1}H NMR (400 MHz, DMSO-d_6) δ [ppm]: 10.08 (s, 1H, N*H* thiourea), 10.01 (s, 1H, N*H* thiourea), 7.90 ((m(AA'BB'), 2H, C*H* anilide), 7.72 ((m(AA'BB'), 2H, C*H* anilide), 7.49 (m, 2H, C*H* phenylthiourea), 7.36 (m, 2H, C*H* phenylthiourea), 7.20 – 6.96 (m, 3H, C*H* benzyl, 1H CH phenylthiourea), 3.53–3.47 (m, 2H, C*H*$_2$ benzyl), 3.03–2.87 (m, 2H, CH$_2$C*H*$_2$CH$_2$ piperidine), 2.81–2.71 (m, 1H, C*H*$_2$CO), 2.64–2.54 (m, 1H, C*H*$_2$CO), 2.22 (s, 3H, C*H*$_3$ benzyl), 2.09 (m, 2H, NC*H*$_2$CH$_2$ piperidine) 1.95 (m, 1H, C*H* piperidine), 1.75–1.58 (m, 2H, NC*H*$_2$CH piperidine), 1.52–1.40 (m, 1H, CH$_2$C*H*$_2$CH piperidine), 1.15–1.08 (m, 1H, CH$_2$C*H*$_2$CH piperidine). ^{13}C NMR (101 MHz, DMSO) δ [ppm]: 179.5 (*C*S), 179.2 (O*C*N oxadiazole), 170.5 (N*C*N oxadiazole), 159.6 (d, ^{1}J(C,F) = 241.3 Hz, *C*F benzyl), 142.5 (*C*N phenyl), 139.5 (d, ^{3}J(C,F) = 5.1 Hz, *C*H$_{meta}$ benzyl), 139.3 (*C*N anilide), 128.6 (*C*H anilide), 127.3 (*C*H phenyl), 126.3 (d, ^{3}J(C,F) = 9.0 Hz, *C*CH$_2$ benzyl), 125.5 (d, ^{4}J(C,F) = 3.0 Hz, *C*H$_{para}$ benzyl), 124.8 (d, ^{2}J(C,F) = 16.1 Hz, *C*H$_{ortho}$ benzyl), 123.8 (*C*H anilide), 123.1 (*C*H phenyl), 121.5 (*C*H phenyl), 113.6 (d, ^{2}J(C,F) = 23.2 Hz, CH$_3$*C* benzyl), 60.2 (N*C*H$_2$ benzyl), 58.3 (N*C*H$_2$ piperidine), 53.5 (N*C*H$_2$ piperidine), 34.1 (CO*C*H$_2$ piperidine), 29.9 (*C*H$_2$ piperidine), 28.6 (*C*H$_2$ piperidine), 24.2

(*C*H piperidine), 10.0 (d, ^{3}J(C,F) = 5.63, *C*H$_3$). HRMS (ESI): m/z calcd. for $C_{29}H_{30}FN_5OS$ + H^+ $[M+H]^+$ 516.22, found 516.22. HPLC analysis: retention time = 16.704 min; peak area, 95 %.

Synthesis of 1-(4-(5-((1-(3-fluoro-2-methylbenzyl) piperidin-3-yl) methyl)-1,2,4-oxadiazol-3-yl) phenyl)-3-(phenyl or benzyl) ureas (9-11). 1 Equivalent of (4-(5-((1-(3-fluoro-2-methylbenzyl)piperidin-3-yl)methyl)-1,2,4-oxadiazol-3-yl)phenyl) aniline **6** was dissolved in CH_2Cl_2 (1.3 mL). 1.2 Equivalent of the corresponding isocyanate was slowly added via syringe to the stirred solution. The reaction mixture was stirred at room temperature for 4 h and afterwards the solvent was evaporated.

*Synthesis of 1-[4-(5-((1-(3-fluoro-2-methylbenzyl)piperidin-3-yl)methyl)-1,2,4-oxadiazol-3-yl) phenyl]-3-(benzyl)urea (**9**).* The crude was purified by flash chromatography on SiO_2 gel with CH_2Cl_2/MeOH (9/1) to afford **9**. White crystalline solid; 80 mg, yield 54 %. R_f = 0.40 (10 % MeOH in CH_2Cl_2). ^{1}H NMR (400 MHz, DMSO-d_6) δ[ppm]: 8.95 (s, 1H, N*H* urea), 7.81 ((m(AA'BB'), 2H, C*H* anilide), 7.59 ((m(AA'BB'), 2H, C*H* anilide), 7.36–7.29 (m, 4H, C*H* benzyl), 7.27–7.22 (m, 1H, C*H* benzyl), 7.15–6.98 (m, 3H, C*H* fluoro-benzyl), 6.76 (t, ^{3}J(H,H) = 7.9 Hz, 1H, N*H* urea), 4.32 (d, ^{3}J(H,H) = 7.9 Hz, 2H, NCH_2 benzyl), 3.41 (s, 2H, CH_2 benzyl), 2.98–2.86 (m, 2H, $CH_2CH_2CH_2$ piperidine), 2.76–2.73 (m, 1H, CH_2CO), 2.60–2.54 (m, 1H, CH_2CO), 2.21 (s, 3H, CH_3 benzyl), 2.08–2.03 (m, 2H, NCH_2CH_2 piperidine), 1.94–1.89 (m, 1H, C*H* piperidine), 1.71–1.59 (m, 2H, NCH_2CH piperidine), 1.49-1.40 (m, 1H, CH_2CH_2CH piperidine), 1.17- 1.08. (m, 1H, CH_2CH_2CH piperidine). ^{13}C NMR (101 MHz, DMSO-d_6) δ [ppm]: 178.8 (*C*O), 167.2 (O*C*N oxadiazole), 160.7 (d, ^{1}J(C,F) = 244.4 Hz, *C*F fluoro-benzyl), 154.9 (N*C*N oxadiazole), 143.4 (*C*NH anilide), 140.1 (*C*CH_2 benzyl), 139.4 (d, ^{3}J(C,F) = 3.9 Hz, *C*H$_{meta}$ benzyl), 128.3 (2C, *C*H benzyl), 127.8 (2C, *C*H anilide), 127.1 (2C, *C*H benzyl), 126.8 (*C*H benzyl), 126.3 (d, ^{3}J(C,F) = 8.8 Hz, *C*CH_2 benzyl), 125.4 (d, ^{4}J(C,F) = 2.4 Hz, *C*H$_{para}$ benzyl),

123.7 (d, ^{2}J(C,F) = 16.0 Hz, *C*H$_{ortho}$ benzyl), 118.5 (*C*C anilide), 117.5 (2C, *C*H anilide), 113.5 (d, ^{2}J(C,F) = 23.1 Hz, CH$_3$*C* benzyl), 60.1 (N*C*H$_2$ benzyl), 58.3 (N*C*H$_2$ piperidine) 53.4 (N*C*H$_2$ piperidine), 42.7 (N*C*H$_2$ benzyl), 34.1 (*C*H$_2$CO), 29.9 (*C*H$_2$, piperidine), 29.7 (*C*H$_2$, piperidine), 24.1 (*C*H piperidine), 10.0 (d, ^{3}J(C,F) = 6.0 Hz, *C*H$_3$). ^{19}F NMR (376 MHz, DMSO-d_6) δ [ppm]: -117.7 (m, C*F*). HRMS (ESI): m/z calcd. for $C_{30}H_{32}FN_5O_2$ + H^+ $[M+H]^+$ 514.25, found 514.26. HPLC analysis: retention time = 15.805 min; peak area, 96 %.

*Synthesis of 1-[4-(5-((1-(3-fluoro-2-methylbenzyl)piperidin-3-yl)methyl)-1,2,4-oxadiazol-3-yl) phenyl]-3-[(4-methoxy)phenyl]urea (**10**).* The crude was purified by flash chromatography on SiO_2 gel with CH_2Cl_2/MeOH (95/5), to obtain the urea (**10**). White crystalline solid, 106 mg, yield 78 %. R_f = 0.44 (10 % MeOH in CH_2Cl_2). ^{1}H NMR (400 MHz, DMSO-d_6) δ [ppm]: 8.96 (s, 1H, N*H*, urea), 8.60 (s, 1H, N*H*, urea), 7.86 ((m(AA'BB'), 2H, C*H* anilide), 7.62 ((m(AA'BB'), 2H, C*H* anilide), 7.38 ((m(AA'XX'), 2H, C*H* 4-OMe-anilide), 7.17–6.99 (m, 3H, C*H* benzyl), 6.88 ((m(AA'XX'), 2H, C*H* 4-OMe-anilide), 3.72 (s, 3H, OC*H*$_3$), 3.42 (s, 2H, C*H*$_2$ benzyl), 3.00– 2.88 (m, 2H, CH$_2$C*H*$_2$CH$_2$ piperidine), 2.77–2.75 (m, 1H, C*H*$_2$CO), 2.65–2.56 (m, 1H, C*H*$_2$CO), 2.22 (s, 3H, C*H*$_3$ benzyl), 2.13–2.04 (m, 2H, NC*H*$_2$CH$_2$ piperidine), 1.97–1.91 (m, 1H, C*H* piperidine), 1.74–1.59 (m, 2H, NC*H*$_2$CH piperidine), 1.51–1.41 (m, 1H, CH$_2$C*H*$_2$CH piperidine), 1.19–1.11. (m, 1H, CH$_2$C*H*$_2$CH piperidine). ^{13}C NMR (101 MHz, DMSO-d_6) δ [ppm]: 178.9 (*C*O), 167.2 (O*C*N oxadiazole), 159.5 (d, ^{1}J(C,F) = 209.0 Hz, *C*F benzyl), 152.5 (N*C*N oxadiazole), 142.9 (*C*NH anilide), 139.4 (d, ^{3}J(C,F) = 3.9 Hz, *C*H$_{meta}$ benzyl), 132.4 (*C*OCH$_3$ 4-OMe-anilide), 127.8 (2C, *C*H anilide), 126.3 (d, ^{3}J(C,F) = 9.0 Hz, *C*CH$_2$ benzyl), 125.4 (d, ^{4}J (C,F) = 2.4 Hz, *C*H$_{para}$ benzyl), 123.5 (d, ^{2}J(C,F) = 16.0 Hz, *C*H$_{ortho}$ benzyl), 120.2 (2C, *C*H 4-OMe-anilide), 119.0 (*C*C anilide), 118.1 (*C*NH 4-OMe-anilide), 117.9 (2C, *C*H anilide), 114.0 (2C, *C*H 4-OMe-anilide), 113.6 (d, ^{2}J(C,F) = 23.5 Hz, CH$_3$*C* benzyl), 60.2 (N*C*H$_2$ benzyl), 55.2 (N*C*H$_2$ piperidine), 53.4

(N*C*H$_2$ piperidine), 48.6 (O*C*H$_3$), 34.1 (CO*C*H$_2$), 30.0 (*C*H$_2$ piperidine), 29.6 (*C*H$_2$ piperidine), 24.8 (*C*H piperidine), 10.0 (d, ^{3}J(C,F) = 5.0 Hz, *C*H$_3$). ^{19}F NMR (376 MHz, DMSO-*d*$_6$) δ [ppm]: -117.7 (m, C*F*). LRMS (APCI): m/z calcd. for $C_{22}H_{25}FN_4O$ + H^+ $[M+H]^+$ 529.6, found 529.8. HPLC analysis: retention time = 15.723 min; peak area, 100 %.

*Synthesis of 1-(4-(5-((1-(3-fluoro-2-methylbenzyl)piperidin-3-yl)methyl)-1,2,4-oxadiazol-3-yl) phenyl)-3-phenylurea (**11**).* The crude was then purified by flash chromatography on SiO_2 gel with CH_2Cl_2/MeOH (96/4), leading to **11**. White crystalline solid, 76 mg, yield 59 %. R_f = 0.34 (10 % MeOH in CH_2Cl_2). ^{1}H NMR (400 MHz, DMSO-*d*$_6$) δ [ppm]: 9.07 (s, 1H, NH urea), 8.82 (s, 1H, NH urea), 7.86 ((m(AA'BB'), 2H, C*H* anilide), 7.62 ((m(AA'BB'), 2H, C*H* anilide), 7.47 (m, 2H, C*H* phenyl), 7.29 (m, 2H, phenyl), 7.17–7.10 (m, 1H, phenyl), 7.08–6.98 (m, 3H, C*H* benzyl), 3.42 (s, 2H, C*H*$_2$ benzyl), 3.00–2.87 (m, 2H, CH$_2$C*H*$_2$CH$_2$ piperidine), 2.76–2.74 (m, 1H, C*H*$_2$CO), 2.63–2.56 (m, 1H, C*H*$_2$CO), 2.22 (s, 3H, C*H*$_3$ benzyl), 2.11–2.05 (m, 2H, NC*H*$_2$CH$_2$ piperidine), 1.98–1.89 (m, 1H, C*H* piperidine), 1.73–1.58 (m, 2H, NC*H*$_2$CH piperidine), 1.52–1.39 (m, 1H, CH$_2$C*H*$_2$CH piperidine), 1.20–1.07 (m, 1H, CH$_2$C*H*$_2$CH piperidine). ^{13}C NMR (101 MHz, DMSO-*d*$_6$) δ [ppm]: 179.2 (*C*O), 167.6 (O*C*N oxadiazole), 161.13 (d, ^{1}J(C,F) = 242.4 Hz, *C*F benzyl), 152.7 (N*C*N oxadiazole), 143.1 (*C*NH anilide), 139.8 (d, ^{3}J(C,F) = 5.0 Hz, *C*H$_{meta}$ benzyl), 129.2 (2C, *C*H phenyl), 128.2 (2C, *C*H anilide), 126.7 (d, ^{3}J(C,F) = 9.0 Hz, *C*CH$_2$ benzyl), 125.8 (d, ^{4}J(C,F) = 3.0 Hz, *C*H$_{para}$ benzyl), 124.1 (d, ^{2}J(C,F) = 16.1 Hz, *C*H$_{ortho}$ benzyl), 122.4 (*C*H phenyl), 119.6 (2 C, *C*NH phenyl and *C*C anilide), 118.7 (2C, *C*H phenyl), 118.4 (2C, *C*H anilide), 113.8 (d, ^{2}J(C,F) = 23.2 Hz, CH$_3$*C* benzyl), 60.5 (N*C*H$_2$ benzyl), 58.7 (N*C*H$_2$ piperidine), 53.8 (N*C*H$_2$ piperidine), 34.5 (CO*C*H$_2$), 30.3 (*C*H$_2$ piperidine), 30.1 (*C*H$_2$ piperidine), 24.5 (*C*H piperidine), 10.4 (d, ^{3}J(C,F) = 5.1 Hz, *C*H$_3$). ^{19}F NMR (376 MHz, DMSO-*d*$_6$) δ [ppm]: -117.7 (m,

C*F*). HRMS (ESI): m/z calcd. for $C_{29}H_{30}FN_5O_2$ + H^+ $[M+H]^+$ 500.24, found 500.24. HPLC analysis: retention time = 16.240 min; peak area, 99 %.

Synthesis of N-(4-(5-((1-(3-fluoro-2-methylbenzyl) piperidin-3-yl)methyl)-1,2,4-oxadiazol-3-yl)phenyl)-2-(4 or 3-X-phenyl) acylamides or benzamides (12-17). A solution of the corresponding acyl chloride (1.0 equiv.) in CH_2Cl_2 (1.1 mL) was added dropwise to a well-stirred mixture of (4-(5-((1-(3-fluoro-2-methylbenzyl)piperidin-3-yl)methyl)-1,2,4-oxadiazol-3-yl)phenyl)aniline **6** (1.0 equiv.) in CH_2Cl_2 (1.1 mL) and 1.1 mL of Na_2CO_3 *aq.* so (10 %). The mixture was stirred for 4-6 hours at room temperature. The organic phase was separated and extracted with brine (3x1.1 mL), dried over $MgSO_4$, filtered and the solvent evaporated under reduced pressure.

*Synthesis of N-(4-(5-((1-(3-fluoro-2-methylbenzyl)piperidin-3-yl)methyl)-1,2,4-oxadiazol-3-yl) phenyl)-2-(4-methoxyphenyl)acetamide (**12**).* The crude was purified by flash chromatography on SiO_2 gel with CH_2Cl_2/MeOH (95/5), to afford **12**. White crystalline solid; 78 mg, yield 60 %. R_f = 0.54 (10 % MeOH in CH_2Cl_2). ^{1}H NMR (400 MHz, DMSO-d_6) δ [ppm]: 10.41 (s, 1H, N*H*, amide), 7.89–7.87 ((m(AA'BB'), 2H, C*H* anilide), 7.78–7.76 ((m(AA'BB'), 2H, C*H* anilide), 7.27–7.25 ((m(AA'XX'), 2H, C*H* benzyl), 7.15–7.09 (m, 1H, C*H* fluoro-benzyl), 7.06–6.97 (m, 2H, C*H* fluoro-benzyl), 6.90–6.88 ((m(AA'XX'), 2H, C*H* benzyl), 3.73 (s, 3H, OCH_3), 3.60 (s, 2H, COCH_2), 3.41 (s, 2H, CH_2 benzyl), 2.99–2.86 (m, 2H, $CH_2CH_2CH_2$ piperidine), 2.75–2.73 (m, 1H, CH_2CO), 2.59–2.54 (m, 1H, CH_2CO), 2.21 (s, 3H, CH_3 benzyl), 2.08–2.07 (m, 2H, NCH_2CH_2 piperidine), 1.94–1.91 (m, 1H, C*H* piperidine), 1.71–1.60 (m, 2H, NCH_2CH piperidine), 1.49–1.39 (m, 1H, CH_2CH_2CH piperidine), 1.16–1.09 (m, 1H, CH_2CH_2CH piperidine). ^{13}C NMR (101 MHz, DMSO-d_6) δ [ppm]: 179.0 (*C*O), 169.9 (*C*OCH_3 benzyl), 167.1 (O*C*N oxadiazole), 160.7 (d, ^{1}J(C,F) = 242.4 Hz, *C*F benzyl), 158.0 (N*C*N oxadiazole), 142.0 (*C*NH anilide), 139.4

(d, ^{3}J(C,F) = 4.0 Hz, *C*H$_{meta}$ benzyl), 130.1 (2C, *C*H benzyl), 127.7 (2C, *C*H anilide), 127.6 (*C*CH$_2$ benzyl), 126.3 (d, ^{3}J(C,F) = 9.0 Hz, *C*CH$_2$ benzyl), 125.4 (d, ^{4}J(C,F) = 2.0 Hz, *C*H$_{para}$ benzyl), 123.7 (d, ^{2}J(C,F) = 16.1 Hz, *C*H$_{ortho}$ benzyl), 120.7 (*C*C anilide), 119.1 (2C, *C*H anilide), 113.7 (2C, *C*H benzyl), 113.4 (d, ^{2}J(C,F) = 22.2 Hz, CH$_3$*C* benzyl), 60.1 (N*C*H$_2$ benzyl), 58.3 (N*C*H$_2$ piperidine), 55.0 (O*C*H$_3$), 53.4 (N*C*H$_2$ piperidine), 42.5 (CO*C*H$_2$ benzyl), 34.0 (CO*C*H$_2$), 29.8 (*C*H$_2$ piperidine), 29.7 (*C*H$_2$ piperidine), 24.1 (*C*H piperidine), 10.0 (d, ^{3}J(C,F) = 6.0 Hz, *C*H3). ^{19}F NMR (376 MHz, DMSO-d_6) δ [ppm]: 117.7 (m, C*F*). HRMS (ESI): m/z calcd. for $C_{31}H_{33}FN_4O_3$ + H^+ $[M+H]^+$ 529.63, found 529.26. HPLC analysis: retention time = 16.093 min; peak area, 98 %.

*Synthesis of N-(4-(5-((1-(3-fluoro-2-methylbenzyl)piperidin-3-yl)methyl)-1,2,4-oxadiazol-3-yl) phenyl)-4-methoxybenzamide (**13**).* The crude was purified by flash chromatography on SiO_2 gel with Cy/ AcOEt (1/1) to afford **13**. White crystalline solid; 48 mg, yield 48 %. R_f = 0.51 (50 % AcOEt in Cy). ^{1}H NMR (400 MHz, DMSO-d_6) δ [ppm]: 10.39 (s, 1H, N*H* amide), 8.00 ((m(AA'XX'), 2H, C*H* benzamide), 7.99 ((m(AA'BB'), 2H, C*H* anilide), 7.93 ((m(AA'BB'), 2H, C*H* anilide,), 7.19–6.98 (m, 3H, C*H* benzyl), 7.09 ((m(AA'XX'), 2H, C*H* benzamide), 3.86 (s, 3H, OC*H*$_3$), 3.43 (s, 2H, C*H*$_2$ benzyl), 3.01–2.89 (m, 2H, CH$_2$C*H*$_2$CH$_2$ piperidine), 2.79–2.75 (m, 1H, C*H*$_2$CO), 2.64–2.58 (m, 1H, C*H*$_2$CO), 2.23 (s, 3H, C*H*$_3$ benzyl), 2.13–2.07 (m, 2H, NC*H*$_2$CH$_2$ piperidine), 1.97–1.91 (m, 1H, C*H* piperidine), 1.75–1.61 (m, 2H, NC*H*$_2$CH piperidine), 1.52–1.42 (m, 1H, CH$_2$C*H*$_2$CH piperidine), 1.20–1.11(m, 1H, CH$_2$C*H*$_2$CH piperidine). ^{13}C NMR (101 MHz, DMSO-d_6) δ [ppm]: 179.4 (*C*O), 167.5 (O*C*N oxadiazole), 165.5 (N*C*N oxadiazole), 162.5 (*C*OCH$_3$ phenyl), 161.1 (d, ^{1}J(C,F) = 242.4 Hz, *C*F benzyl), 142.6 (*C*NH anilide), 139.8 (d, ^{3}J(C,F) = 4.0 Hz, *C*H$_{meta}$ benzyl), 130.1 (2C, *C*H benzamide), 127.9 (2C, *C*H anilide), 127.0 (*C*CO, benzamide), 126.7 (d, ^{3}J(C,F) = 9.0 Hz, *C*CH$_2$ benzyl), 125.8 (d, ^{4}J(C,F) = 3.0 Hz, *C*H$_{para}$

benzyl), 124.1 (d, ^{2}J(C,F) = 16.1 Hz, *C*H$_{ortho}$ benzyl), 121.2 (*C*C anilide), 120.6 (2C, *C*H anilide), 114.0 (2C, *C*H benzamide), 113.8 (d, ^{2}J(C,F) = 24.2 Hz, CH$_3$*C* benzyl), 60.5 (N*C*H$_2$ benzyl), 58.7 (N*C*H$_2$ piperidine), 55.8 (O*C*H$_3$), 53.8 (N*C*H$_2$, piperidine), 34.5 (CO*C*H$_2$), 30.3 (*C*H$_2$ piperidine), 30.1 (*C*H$_2$ piperidine), 24.5 (*C*H piperidine), 10.4 (d, ^{3}J(C,F) = 5.0 Hz, *C*H$_3$). ^{19}F NMR (376 MHz, DMSO-*d*$_6$) δ [ppm]: -117.7 (m, C*F*). LRMS (APCI): m/z calcd. for $C_{30}H_{31}FN_4O_3$ + H^+ $[M+H]^+$ 514.6, found 514.1. HPLC analysis: retention time = 16.125 min; peak area, 97 %.

*Synthesis of 4N-(4-(5-((1-(3-fluoro-2-methylbenzyl)piperidin-3-yl)methyl)-1,2,4-oxadiazol-3-yl) phenyl)-3-methoxybenzamide (**14**).* The crude was purified by flash chromatography on SiO_2 gel with Cy / AcOEt (1/1) to obtain **14**. Yellow oil; 61 mg, yield 90 %. R_f = 0.16 (50 % AcOEt in Cy). ^{1}H NMR (400 MHz, DMSO-*d*$_6$) δ [ppm]: 10.51 (s, 1H, N*H* amide), 7.99 ((m(AA'BB'), 2H, C*H* anilide), 7.95 ((m(AA'BB'), C*H* anilide), 7.57 (m, 1H, C*H* benzamide), 7.52 (m, 1H, C*H* benzamide), 7.48 (m, 1H, C*H* benzamide), 7.20 (m, 1H, C*H* benzamide), 7.15-7.00 (m, 3H, C*H* benzyl), 3.86 (s, 3H, C*H*$_3$ methoxy), 3.44 (s, 2H, C*H*$_2$ benzyl), 3.02-2.90 (m, 2H, CH$_2$C*H*$_2$CH$_2$ piperidine), 2.81-2.75 (m, 1H, C*H*$_2$CO), 2.64-2.59 (m, 1H, C*H*$_2$CO), 2.23 (s, 3H, C*H*$_3$ benzyl), 2.14-2.06 (m, 2H, NC*H*$_2$CH$_2$ piperidine), 1.97-1.90 (m, 1H, C*H* piperidine), 1.76-1.62 (m, 2H, NC*H*$_2$CH piperidine), 1.53-1.43 (m, 1H, CH$_2$C*H*$_2$CH piperidine), 1.15-1.10 (m, 1H, CH$_2$C*H*$_2$CH piperidine). ^{13}C NMR (101 MHz, DMSO-d$_6$): δ [ppm]: 179.4 (*C*O), 167.5 (O*C*N oxadiazole), 165.9 (O*C*N oxadiazole), 161.1 (d, ^{1}J(C,F) = 241.4 Hz, *C*F benzyl), 159.6 (*C*OCH$_3$ phenyl), 142.3 (*C*NH anilide), 139.8 (d, ^{3}J(C,F) = 4.0 Hz, *C*H$_{meta}$ benzyl), 136.4 (*C*H benzamide), 130.0 (CO*C* benzamide), 128.0 (2C, *C*H anilide), 126.6 (d, ^{3}J(C,F) = 9.0 Hz, *C*CH$_2$ benzyl), 125.8 (d ^{4}J (C,F) = 3.0 Hz, *C*H$_{para}$ benzyl), 124.1 (d, ^{2}J(C,F) = 16.1 Hz, *C*H$_{ortho}$ benzyl), 121.5 (C*C*, anilide), 120.7 (2C, *C*H anilide), 120.3 (*C*H benzamide), 117.9 (*C*H benzamide), 113.8 (d, ^{2}J(C,F) = 23.2 Hz, CH$_3$*C* benzyl), 113.4 (*C*H benzamide), 60.5 (N*C*H$_2$ benzyl), 58.6 (N*C*H$_2$,

piperidine), 55.7 (O*C*H$_3$), 53.8 (N*C*H$_2$, piperidine), 34.4 (CO*C*H$_2$), 30.3 (*C*H$_2$ piperidine), 30.1 (*C*H$_2$ piperidine), 24.5 (*C*H piperidine), 10.4 (d, ^{3}J(C,F) = 6.0 Hz, *C*H$_3$). ^{19}F NMR (376 MHz, DMSO-*d*$_6$) δ [ppm]: -117.7 (m, C*F*). LRMS (APCI): m/z calcd. for $C_{31}H_{32}FN_3O_3$ + H^+ $[M+H]^+$ 514.6, found 514.4. HPLC analysis: retention time = 19.123 min; peak area, 98 %.

*Synthesis of 4-fluoro-N-(4-(5-((1-(3-fluoro-2-methylbenzyl)piperidin-3-yl)methyl)-1,2,4-oxadiazol-3-yl)phenyl)benzamide (**15**).* The crude was purified by flash chromatography on SiO_2 gel with Cy / AcOEt (1/1), leading to **15**. White crystalline solid; 60 mg, yield 91 %. R_f = 0.69 (50 % AcOEt in Cy). ^{1}H NMR (400 MHz, DMSO-*d*$_6$) δ [ppm]: 10.55 (s, 1H, N*H* amide), 8.08 ((m(AA'XX'), 2H, C*H* benzamide), 7.99 ((m(AA'BB'), 2H, C*H* anilide), 7.95 ((m(AA'BB'), 2H, C*H* anilide), 7.41 ((m(AA'XX'), 2H, C*H* benzamide), 7.17–7.00 (m, 3H, C*H* benzyl), 3.44 (s, 2H, C*H*$_2$ benzyl), 3.02–2.90 (m, 2H, CH$_2$C*H*$_2$CH$_2$ piperidine), 2.80–2.75 (m, 1H, C*H*$_2$CO), 2.65–2.59 (m, 1H, C*H*$_2$CO), 2.23 (s, 3H, C*H*$_3$ benzyl), 2.15–2.06 (m, 2H, NC*H*$_2$CH$_2$ piperidine), 1.99–1.91 (m, 1H, C*H* piperidine), 1.76–1.60 (m, 2H, NC*H*$_2$CH piperidine), 1.52–1.43 (m, 1H, CH$_2$C*H*$_2$CH piperidine), 1.21–1.11 (m, 1H, CH$_2$C*H*$_2$CH piperidine). ^{13}C NMR (101 MHz, DMSO-*d*$_6$) δ [ppm]: 179.4 (*C*O), 167.5 (O*C*N oxadiazole), 165.1 (N*C*N oxadiazole), 164.6 (d, ^{1}J(C,F) = 250.5 Hz, *C*F benzamide), 161.1 (d, ^{1}J(C,F) = 241.4 Hz, *C*F benzyl), 142.3 (*C*NH anilide), 139.8 (d, ^{3}J(C,F) = 4.0 Hz, *C*H$_{meta}$ benzyl), 131.4 (d, ^{4}J(C,F) = 3.0 Hz, CO*C* benzamide), 131.0 (d, ^{3}J(C,F) = 9.0 Hz, 2C, *C*H benzamide), 128.0 (2C, *C*H anilide), 126.6 (d, ^{3}J(C,F) = 8.0 Hz, *C*CH$_2$ benzyl), 125.8 (d, ^{4}J(C,F) = 3.0 Hz, *C*H$_{para}$ benzyl), 124.1 (d, ^{2}J(C,F) = 16.1 Hz, *C*H$_{ortho}$ benzyl), 121.6 (C*C* anilide), 120.7 (2C, *C*H anilide), 115.8 (d, ^{2}J(C,F) = 22.2 Hz, 2C, *C*H benzamide), 113.8 (d, ^{2}J(C,F) = 23.2 Hz, CH$_3$*C* benzyl), 60.5 (N*C*H$_2$ benzyl), 58.7 (N*C*H$_2$, piperidine), 53.8 (N*C*H$_2$, piperidine), 34.4 (CO*C*H$_2$), 30.3 (*C*H$_2$ piperidine), 30.1 (*C*H$_2$ piperidine), 24.5 (*C*H piperidine), 10.4 (d, ^{3}J(C,F) = 5.0 Hz, *C*H$_3$). ^{19}F NMR (376 MHz, DMSO-*d*$_6$) δ [ppm]: -

117.7 (m, C*F* benzyl), -108.3 (m, C*F* benzamide). LRMS (APCI): m/z calcd. for $C_{29}H_{28}F_2N_4O_2$ + H^+ $[M+H]^+$ 502.5, found 503.0. HPLC analysis: retention time = 19.218 min; peak area, 97.9 %. Enantiomers of compound **15** were isolated via chiral chromatography as white crystalline solid. For conditions applied, see materials and methods above. HPLC analysis: Enantiomer 1, retention time = 49.657 min; peak area, 98.7 %. Enantiomer 2, retention time = 53.323: peak area, 98.5 %. Isolated enantiomers were further analyzed via circular dichroism. In a quartz cell (1 mm width), 1 mM solution in methanol was added and the absorption and circular dichroism were measured in the UV-vis range of 220-380 nm at 20 °C with a speed of 500 nm/min (5 accumulations). At 285 nm wavelength, the same maximum absorption was observed for the racemate and two isolated enantiomers. CD measurement: Enantiomer 1: + 1.3 mdeg, Enantiomer 2: -1.4 mdeg.

*Synthesis of 4-chloro-N-(4-(5-((1-(3-fluoro-2-methylbenzyl)piperidin-3-yl)methyl)-1,2,4-oxadiazol-3-yl)phenyl)benzamide (**16**).* The crude was purified by flash chromatography on SiO_2 gel with Cy / AcOEt (1/1), yielding **16**. White crystalline solid; 63 mg, yield 90 %. R_f = 0.34 (50 % AcOEt in Cy). ^{1}H NMR (400 MHz, DMSO-d_6) δ [ppm]: 10.59 (s, 1H, N*H* amide), 8.02 ((m(AA'XX'), 2H, C*H* benzamide), 7.99 ((m(AA'BB'), 2H, C*H* anilide), 7.95 ((m(AA'BB'), 2H, C*H* anilide), 7.64 ((m(AA'XX'), 2H, C*H* benzamide), 7.16–6.99 (m, 3H, C*H* benzyl), 3.43 (s, 2H, CH_2 benzyl), 3.01–2.89 (m, 2H, $CH_2CH_2CH_2$ piperidine), 2.80–2.75 (m, 1H, CH_2CO), 2.63–2.57 (m, 1H, CH_2CO), 2.23 (s, 3H, CH_3 benzyl), 2.14–2.04 (m, 2H, NCH_2CH$_2$ piperidine), 1.96–1.90 (m, 1H, C*H* piperidine), 1.76–1.61 (m, 2H, NCH_2CH piperidine), 1.52–1.41 (m, 1H, CH_2CH_2CH piperidine), 1.20–1.10 (m, 1H, CH_2CH_2CH piperidine). ^{13}C NMR (101 MHz, DMSO-d_6) δ [ppm]: 179.4 (*C*O), 167.5 (O*C*N oxadiazole), 165.1 (N*C*N oxadiazole), 161.13 (d, ^{1}J(C,F) = 242.4 Hz, *C*F benzyl), 142.2 (*C*NH anilide), 139.8 (d, ^{3}J(C,F) = 4.0 Hz, *C*H$_{meta}$ benzyl), 137.0 (*C*Cl, benzamide), 133.7 (CO*C* benzamide), 130.1 (2C, *C*H benzamide), 128.9 (2C, *C*H benzamide), 128.0 (2C, *C*H

anilide), 126.6 (d, ^{3}J(C,F) = 9.0 Hz, *C*CH$_2$ benzyl), 125.8 (d, ^{4}J(C,F) = 2.02 Hz, *C*H$_{para}$ benzyl), 124.1 (d, ^{2}J(C,F) = 16.1 Hz, *C*H$_{ortho}$ benzyl), 121.7 (C*C* anilide), 120.7 (2C, *C*H anilide), 113.8 (d, ^{2}J(C,F) = 23.2 Hz, CH$_3$*C* benzyl), 60.5 (N*C*H$_2$ benzyl), 58.7 (N*C*H$_2$, piperidine), 53.8 (N*C*H$_2$, piperidine), 34.4 (CO*C*H$_2$), 30.3 (*C*H$_2$ piperidine), 30.1 (*C*H$_2$ piperidine), 24.5 (*C*H piperidine), 10.4 (d, ^{3}J(C,F) = 5.0 Hz, *C*H$_3$). ^{19}F NMR (376 MHz, DMSO-*d*$_6$) δ [ppm]: -117.7 (m, C*F*). HRMS (ESI): m/z calcd. for $C_{29}H_{28}FClN_4O_2$ + H^+ $[M+H]^+$ 519.2, found 519.2, 521.2. HPLC analysis: retention time = 20.361 min; peak area, 99 %.

*Synthesis of 5-chloro-N-(4-(5-((1-(3-fluoro-2-methylbenzyl)piperidin-3-yl)methyl)-1,2,4-oxadiazol-3-yl)phenyl) thiophene-2-carboxamide (**17**).* The crude was purified by flash chromatography on SiO_2 gel with Cy / AcOEt (1/1) to obtain **17**. White crystalline solid; 89 mg, yield 66 %. R_f = 0.62 (50 % AcOEt in Cy). ^{1}H NMR (400 MHz, DMSO-*d*$_6$) δ [ppm]: 10.57 (s, 1H, N*H*, amide), 7.98 (d, ^{3}*J*(H,H) = 5.6 Hz, 1H, C*H* thiophene), 7.96 ((m(AA'BB'), C*H* anilide), 7.91 ((m(AA'BB'), 2H, C*H* anilide), 7.31 (d, ^{3}*J*(H,H) = 5.5 Hz, 1H, C*H* thiophene), 7.17–6.99 (m, 3H, C*H* benzyl), 3.43 (s, 2H, C*H*$_2$ benzyl), 3.03–2.89 (m, 2H, CH$_2$C*H*$_2$CH$_2$ piperidine), 2.79–2.73 (m, 1H, C*H*$_2$CO), 2.61–2.59 (m, 1H, C*H*$_2$CO), 2.23 (s, 3H, C*H*$_3$ benzyl), 2.13–2.05 (m, 2H, NC*H*$_2$CH$_2$ piperidine), 1.98–1.90 (m, 1H, C*H* piperidine), 1.74–1.60 (m, 2H, NC*H*$_2$CH piperidine), 1.52–1.42 (m, 1H, CH$_2$C*H*$_2$CH piperidine), 1.20–1.10 (m, 1H, CH$_2$C*H*$_2$CH piperidine). ^{13}C NMR (101 MHz, DMSO-*d*$_6$) δ [ppm]: 179.5 (*C*O), 167.4 (O*C*N oxadiazole), 161.1 (d, ^{1}J(C,F) = 241.4 Hz, *C*F benzyl), 159.4 (N*C*N oxadiazole), 141.6 (*C*C anilide), 139.8 (d, ^{3}J(C,F) = 4.0 Hz, *C*H$_{meta}$ benzyl), 139.1 (*C*Cl thiophene), 134.8 (*C*CO thiophene), 130.0 (*C*H thiophene), 128.8 (*C*H thiophene), 128.1 (2C, *C*H anilide), 126.6 (d, ^{3}J(C,F) = 9.0 Hz, *C*CH$_2$ benzyl), 125.8 (d, ^{4}J(C,F) = 3.03 Hz, *C*H$_{para}$ benzyl), 124.1 (d, ^{2}J(C,F) = 16.1 Hz, *C*H$_{ortho}$ benzyl), 121.8 (*C*NH anilide), 120.7 (2C, *C*H anilide), 113.8 (d, ^{2}J(C,F) = 22.2 Hz, CH$_3$*C* benzyl), 60.5 (N*C*H$_2$ benzyl), 58.7 (N*C*H$_2$, piperidine),

53.8 (N*C*H_2, piperidine), 34.4 (CO*C*H_2), 30.3 (*C*H_2 piperidine), 30.1 (*C*H_2 piperidine), 24.7 (*C*H piperidine), 10.4 (d, ^{3}J(C,F) = 5.1 Hz, *C*H_3). LRMS (APCI): m/z calcd. for $C_{27}H_{26}FClN_4O_2S + H^+$ $[M+H]^+$ 525.0, found 524.9, 526.9. HPLC analysis: retention time = 18.005 min; peak area, 97 %.

Molecular docking. The pdb structures of proteins were downloaded from the Protein Data Bank (pdb) database (www.rcsb.org).[78] *Sm*Sirt2 homology model was generated using Swiss-Model server (swissmodel.expasy.org).[79] The human Sirt2 conformation with SirReal ligand (PDB ID 5DY5) was taken for docking and as a template for *Sm*Sirt2 homology model generation, as it could accommodate bulky ligands. Comparison and visualisation of protein-ligand complexes as well as ligand preparation were performed with MOE software (MOE version 2019.01; Chemical Computing Group Inc., Montreal, Canada). Protein preparation and ligand docking was performed with Schrödinger software (Schrödinger Release 2020-2: LigPrep, Schrödinger, LLC: NewYork, NY, 2020). Default procedure was applied for protein preparation using Protein Preparation Wizard - addition of missing hydrogen atoms and amino acid side chains, removal of solvent molecules and metal ions, optimization of protonation states and minimization with OPLS Force Field.[80] Docking was done using Glide in standard precision (SP) mode. The output of the LigPrep was applied to the Confgen tool in Schrödinger Suite by applying 64 conformers per each ligand and minimizing the conformers. Molecular docking studies were performed using the standard precision (SP) mode with flexible ligand sampling and enhanced planarity of the conjugated pi groups in the Glide program of the Schrödinger Suite. The grid box was generated with 15×15×15 Å size using the Receptor Grid Generation module in Schödinger. Redocking procedure was able to reproduce the binding mode of cocrystallized ligand in 5DY5 and 8PY3 with RMSD below 0.3 Å (Fig S2 SI).

Expression and purification of SmSirt2. Overexpression was carried out in E. coli BL21(DE3) cells in 2× Luria Broth medium. The cells were grown to OD600 of 1.2 at 37 °C; then, the culture was cooled down to 25 °C and induction of expression was done by adding 0.5 mM final isopropyl-1-thio-β-D-galactopyranoside (Euromedex), in the presence of 100 µM $ZnCl_2$. Harvested bacteria were resuspended in lysis buffer (400 mM NaCl, 10 mM Tris−HCl pH 8.0) and lysed by sonication. The lysate was clarified by centrifugation (17 000 rpm, JA-25.50 Beckman) for 1 h. The supernatant was loaded onto Talon Metal affinity resin (Clontech) preequilibrated with the lysis buffer. The 3C protease treatment was used to remove the His-tag from the recombinant protein, which was subsequently loaded onto HiLoad 16/60 Superdex 200 gel filtration column (Amersham Bioscience) equilibrated in 400 mM NaCl, 10 mM Tris−HCl pH 8.0, and 2 mM dithiothreitol (DTT). Finally, the protein was concentrated with an Amicon Ultra centrifugal filter unit (Millipore) to reach a final concentration of 1.5 mg/mL as assayed by the A280 measurement (NanoDrop).

Expression and purification of Sirt1 and Sirt2. Chemically competent E. coli BL21 Star (DE3) cells were transformed with the expression vectors pET30S-hSirt1$_{134-747}$ or pET30S-hSirt2$_{56-356}$. The cells were grown at 37 °C in 2× YT medium supplemented with 50 µgmL^{-1} kanamycin to an OD_{600} of 0.6 – 0.7. Overexpression of Sirt1$_{134-747}$ and Sirt2$_{56-356}$ was induced by addition of isopropyl-β-D-1-thiogalactopyranoside (IPTG) to a final concentration of 1 mM. After further cultivation for 16 h at 20 °C, the cells were harvested by centrifugation for 15 min at 5,000 g. The cells were resuspended in lysis buffer (100 mM Tris/HCl buffer at pH=8.0, 150 mM NaCl and 10 % (v/v) glycerol) and disrupted by ultrasonication (Branson Digital Sonifier 250) at 70 % amplitude for 10 min (3 s working, 10 s pause). The cell debris were removed by centrifugation for 1 h at 80,000 g, and the supernatant was loaded on a Strep-Tactin Superflow cartridge (5 ml

bed volume, IBA Lifescience, Germany). After elution with lysis buffer containing D-Desthiobiotin (5 mM, IBA Lifescience, Germany) the target proteins were further purified by size-exclusion chromatography (Superdex S200 26/60, GE Healthcare, IL, USA) equilibrated with Tris/HCl buffer (20 mM, 150 mM NaCl, pH=8.0). Pure protein was concentrated by ultrafiltration, flash-frozen in liquid nitrogen and stored at −80 °C until further use. Purity and identity of the target proteins were verified by SDS-PAGE and protein concentration was determined by the bicinchoninic acid (BCA) method using bovine serum albumin (BSA) as a standard.

Crystallization. For crystallization experiments truncated human $Sirt2_{56\text{-}356}$ was expressed and purified as described previously with minor modifications summarized below.[74] $Sirt2_{56\text{-}356}$ was overexpressed in 2×YT medium (5 g/L NaCl, 16 g/L tryptone, 10 g/L yeast extract) using strain *E. coli* BL21 Star (DE3) at 20 °C overnight. Overexpression was induced with IPTG (Isopropyl-β-D-1-thiogalactopyranoside, final concentration of 1.0 mM) at an OD_{600} of 0.6 – 0.8. The cleavage of the His_{10}-Tag *via* TEV protease was performed in lysis buffer (50 mM Tris/HCl, 500 mM NaCl, 10 % (v/v) glycerol, 0.5 mM Tris(2-carboxyethyl)phosphine (TCEP), pH 8.0) at 4 °C for 36 h. $Sirt2_{56\text{-}356}$ was applied on a HisTrap™ HP column (5 mL, GE Healthcare) again to obtain pure fractions of $Sirt2_{56\text{-}356}$ with cleaved His_{10}-Tag in the flowthrough. For the last purification step a Superdex S75 26/600 gel filtration column (20 mM HEPES, 150 mM NaCl, pH 7.5) was used.

Crystallization assays were set up with the Oryx Nano pipetting robot (Douglas Instruments, East Garston, UK) using the vapor diffusion sitting drop method (MRC 2 Well UVP Plate, SWISSCI, Buckinghamshire, England) at 20 °C. Sirt2 (12.8 mg/mL) was incubated with 1.67 mM compound **16** (100 mM stock solution in DMSO, 1.67 % (v/v) final DMSO concentration) on ice for 1 h prior to crystallization. To remove precipitates, the solutions were centrifuged 10 min at 4 °C before

pipetting. Initial crystals of the Sirt2-**16** complex were only obtained in presence of Sirt2-**Mz242** crystals as microseeds (see **Figure 1** for **Mz242** structure).[81] These crystals formed after 3 days in wells with 0.3 µL protein solution, 0.1 µL Sirt2-**Mz242** crystal solution and 0.3 µL reservoir solution in a condition of 26.5 % (w/v) PEG 3,350 in 0.1 M Bis-Tris at pH 6.5. Suitable crystals of the Sirt2-**16** complex formed after 5 days in wells with 0.3 µL protein solution, 0.1 µL Sirt2-**16** crystal solution and 0.3 µL reservoir solution in a condition of 25 % (w/v) PEG 3,350 in 0.22 M Bis-Tris at pH 6.5. The crystals were cryoprotected with a mixture of reservoir solution and 10 % (v/v) 2*R*,3*R*-(–)-butanediol, mounted on a nylon loop and flash-cooled in liquid nitrogen.

Data collection and structure determination. X-ray diffraction data was collected on ID30A-3 (MASSIF-3) beamline at the European Synchrotron Radiation Facility (ESRF, Grenoble) using an Eiger X 4M detector. The dataset was processed using autoPROC[82] and scaled using Aimless.[83] The structure was solved by molecular replacement with Phaser[84] using the Sirt2-SirReal2-AcLysH3 complex (PDB 4RMH)[74] as a search model. The model was built and refined in iterative steps with COOT[85] and either REFMAC[86] or Phenix.refine[87]. Restraints for **16** were generated with the Grade Web Server (Global Phasing Ltd., United Kingdom). All residues except for Met299, Ile300, Met301, Gly302 and Leu303 of the Sirt2-specific insertion are defined in the electron density. Amino acids Gly101 – Tyr106 and Leu112 – Pro113 exhibit poor electron density and higher *B*-factors (50 – 70 Å²) compared to the rest of the protein (avg. 26.5 Å², Figure S4 (B)). The electron density of **16** is well refined. Final structures were validated using MolProbity.[88] Data collection and refinement statistics are summarized in Table S2.

General biochemistry conditions. The water used for *in vitro* assays was distilled (bidest. H_2O) in a Milli-Q Gradient (Millipore) device. Buffer solutions were prepared from H_2O (bidest.) in 100 mL. Buffer components were dissolved in final concentrations according to the experimental

procedure. The pH was adjusted using a METTLER TOLEDO Benchtop pH Meter, which was calibrated before measurements. After filtration, bottles were stored at 4 °C. Specific detergents and additives like Triton X-100 (TRT-X100), 1,4-dithiothreitol (DTT) and CHAPS were freshly added before performing the experiment. Substrates ZMAL, ZMML, the product AMC, NA, TAMRA-probe and SYPRO™ Orange dye were all stored as DMSO stock in mM range concentration (according to the experimental procedure) at -20 °C and freshly diluted in assay buffer when the assay was conducted. Peptides were stored as 1 mM stock in distilled water and stored at -80 °C. Enzymes Sirt1-3, *Sm*Sirt2 and trypsin were stored in appropriate buffer at -80 °C. Inhibitors were generally stored as 10 mM DMSO stock solutions at -20 °C and diluted in series with assay buffer to specific concentrations according to the testing and in some cases to compound solubility. Testing was conducted in duplicates or triplicates per sample and the experiment was repeated at least two times. The results are reported as mean ± STD of at least two separate independent experiments.

In vitro deacetylation assay for Sirt1-3. According to the previously established protocol[89], The assay was performed in black 96 well plates (OptiPlate TM 96-F, Pinch bar design, Perkin Elmer, USA) with a reaction volume of 60 µL per well. 47 µL $hSirt2_{50\text{-}356}$ in assay buffer (50 mM Tris–HCl, 137 mM NaCl, 2.7 mM KCl, 1 mM $MgCl_2$, pH=8.0) were mixed with 5 µL of a substrate solution (10.5 µM final concentration) and 3 µL of inhibitor dissolved in DMSO at various concentrations or 3 µL of DMSO as control (final assay concentration 5 % (v/v)). 5 µL of NAD^+ solution (3.98 mg/mL in assay buffer, final assay concentration 500 µM) were added in order to start the reaction. The reaction was incubated for 4 h at 37 °C and 250 rpm. hSirt2 assay concentration was adjusted in order to have a final ZMAL conversion between 15 % and 30 %. After the first incubation, 60 µL of stop solution (50 mM Tris, 100 mM NaCl, 6.7 % (v/v) DMSO,

trypsin 1mg/mL, 8 mM nicotinamide, pH=8.0) were added. The microplate was further incubated for 20 min at 37 ºC and 250 rpm. Fluorescence intensity was measured by microplate reader (λ_{Ex} =390 nm, λ_{Em} =460 nm, BMG POLARstar Optima, BMG Labtech, Germany). As blank control a solution containing ZMAL without the enzyme was used. For 100 % theoretical conversion control, AMC was used instead of ZMAL and no enzyme was added. The substrate conversion was evaluated in relation to the 100 % control, after blank subtraction. The inhibition was evaluated in relation to a DMSO control. IC_{50} values were then determined a using non-linear regression fit with Origin Pro 2019 software. All experiments were performed at least in duplicates.

In vitro demyristoylation assay for Sirt2. As previously described[77], the protocol requires the same assay conditions as the end-point homogeneous fluorescence-based assay for hSirt1-3 deacetylation, using ZMML instead of ZMAL as substrate (5.25 µM final assay concentration) and a different buffer composition: 25 mM Hepes 137 mM NaCl, 2.7 mM KCl, 1 mM $MgCl_2$, Triton X-100 0.015 %, pH=8.0. All experiments were performed at least in duplicates.

In vitro activity assay for SmSirt2. The assay was performed as previously described[71]. In 384 well black plates (OptiPlate TM 384-F, Perkin Elmer, USA). 14 µL of *Sm*Sirt2 (*Sm*ST1-N1C1; amino acid residues 21 to 322) in assay buffer (25mM Tris–HCl, 137mM NaCl, 2.7mM KCl, 1mM $MgCl_2$, 0.5mM DTT, 0.015% of TritonX-100, pH=8.0) were mixed with 2.5 µL of substrate solution (12.6 mM stock solution in DMSO diluted with assay buffer to obtain a final assay concentration of 10.5 µM) and 1 µL of inhibitor or 1 µL of DMSO as control (final assay concentration 5 % (v/v)). 2.5 µL of NAD^+ solution (2.653 mg/mL in assay buffer, final assay concentration 500 µM) were added in order to start the reaction. The mixture was then incubated for 1 h at 37 ºC and 250 rpm. *Sm*Sirt2 assay concentration was adjusted in order to have a final

ZMAL conversion between 15 % and 30 %. After the first incubation 20 µL of stop solution (50 mM Tris, 100 mM NaCl, 6.7 % (v/v) DMSO, trypsin 1 mg/mL, 8 mM nicotinamide, pH=8.0) were added. The plate was then incubated for 20 min at 37 °C and 250 rpm. The fluorescence intensity was measured in a microplate reader (λ_{Ex}=390 nm, λ_{Em}=460 nm, BMG POLARstar Optima, BMG Labtech, Germany). As blank control a solution containing ZMAL without the enzyme was used. For 100 % theoretical conversion control, AMC was used instead of ZMAL and no enzyme was added. The substrate conversion was evaluated in relation to the 100 % control, after blank subtraction. The inhibition was evaluated in relation to a DMSO control. IC_{50} values were then determined a using non-linear regression fit with Origin Pro 2019 software. All experiments were performed at least in duplicates.

Thermal shift assay. As previously reported[74], in a black 96 well plates (Hard-Shell® PCR-Plates, thin-wall, BioRAD, USA), 10 µL of hSirt2 (final assay concentration 0.2 $mgmL^{-1}$) in assay buffer (Tris/HCl 25 mM, NaCl 150 mM, Dithiothreitol DTT 1 mM, pH=8.0) were mixed with SYPRO™ Orange (1:4000, Sigma-Aldrich, Germany) with or without NAD^+ (final assay concentration 2.5 mM). 10 µL of the inhibitor was added (final assay concentration 5 or 25 µM) and the fluorescence intensity was monitored during a constant temperature gradient of 1 °C per 20 s from 25 – 95 °C using a real-time PCR machine (C1000 TouchTM Thermal Cycler, CFX96TM Real-Time System, BioRAD, USA). Melting temperatures were determined according to a published procedure[90] using Graphpad Prism software.

Fluorescence polarization assay. According to the published procedure[30], the assay was performed in 384-well black, non-binding microplate (Greiner Bio-One GmbH, Frickenhausen, Germany) with a total assay volume of 20 µL. 4 µL of assay buffer (50 mM TRIS-HCl, 137 mM NaCl, 2.7 mM KCl, 1 mM $MgCl_2$, 1 mg/mL BSA and 0.05 % CHAPS, pH=8.0), 10 µL of hSirt256-

356 (3 mg/mL stock diluted in assay buffer, final assay concentration 200 nM), and 1 µL of sample at different assay concentrations was incubated at 37 °C and 250 rpm for 10 min. 5 µL of SirReal probe solution (prepared from 10 mM stock solution diluted in assay buffer, final assay concentration 40 nM) were then added and the microplate was incubated for 30 minutes at 37 °C and 250 rpm. Fluorescence polarization was then measured by EnVisionTM plate reader (PerkinElmer, optical module – BODIPY TMR FP, excitation filter – FP 531 nm, emission filter 1 – FP p-pol 595 nm, emission filter 2 – FP s-pol 595 nm). For the blank control 19 µL of buffer were incubated with 1 µL of DMSO (final assay concentration 5 % (v/v)). In the minimum control, characterized by complete prevention of fluorescent probe binding, 1 µL of assay buffer was used, while for the maximum control, characterized by complete binding of the fluorescent probe, 1 µL of DMSO was added. Inhibition was calculated using Equation reported below (P_I, P_{neg} and P_{pos} are fluorescence polarization values of samples, positive and negative control respectively). All experiments were performed at least in duplicates.

$$I = 100 \times \left(1\left(\frac{P_I - P_{neg}}{P_{pos} - P_{neg}}\right)\right)\%$$

Progress curve analysis. In a black 96 well plates (OptiPlate TM 96-F, Pinch bar design, Perkin Elmer, USA), 45 µL of a hSirt2$_{56\text{-}356}$ solution (0.7 µL of hSirt2$_{56\text{-}356}$ (3 mg/mL per well) in assay buffer (50 mM Tris–HCl, 137 mM NaCl, 2.7 mM KCl, 1 mM $MgCl_2$, pH=8.0), 5 µL of substrate (100 µM final assay concentration) and 1 µL of DMSO or 60x inhibitor (at various concentrations) were added. 5 µL NAD^+ 3.98 mg/mL (500 µM final assay concentration) and 5 µL trypsin 240 ng/µL assay concentration were then added to start the catalysis. The reaction was monitored over time for 60 min, measuring the fluorescence intensity of AMC released every 30 seconds. The

velocity of each reaction was determined via linear fit using Graphpad Prism software. All experiments were performed at least in duplicates.

Modality of inhibition. In a black 96 well plates (OptiPlate TM 96-F, Pinch bar design, Perkin Elmer, USA), 45 µL of a $hSirt2_{56-356}$ solution (0.7 µL of $hSirt2_{56-356}$ (3 mg/mL per well) in assay buffer (50 mM Tris–HCl, 137 mM NaCl, 2.7 mM KCl, 1 mM $MgCl_2$, pH=8.0), 5 µL of substrate (7.8 µM-1 mM final assay concentration) and 1 µL of DMSO or 60x inhibitor (at various concentrations) were added. 5 µL NAD^+ 3.98 mg/mL (500 µM final assay concentration) and 5 µL of trypsin 240 ng/µL (assay concentration) were then added to start the catalysis. The reaction was monitored over time for 60 min, measuring the fluorescence intensity of AMC released every 30 seconds. The velocity of each reaction was determined via linear fit, maximum velocity and Michaelis-Menten parameters for each inhibitor concentration were obtained with a non-linear Michaelis-Menten fit, using Graphpad Prism software. All experiments were performed at least in duplicates.

Cell viability assay (MTS assay). Cell viability was determined by using the Celltiter 96 Aqueous nonradioactive Proliferation Assay (Promega). Cells were seeded in sterile 96-well plates at a density of 2000 cells per well and incubated for 72 h at 37 °C and 5% CO2. Compound and vehicle were added to a final concentration of 0.5% DMSO. After 72 of incubation time, 20 mL of a mixture (20 : 1) consisting of MTS (3-(4,5-dimethylthiazol-2-yl)- 5-(3-carboxymethoxyphenyl)-2-(4-sulfophenyl-2H-tetrazolium) and PMS (phenazine methosulfate) were added to each well. Absorbance was measured after another 2–4 h with a BMG LABTECH POLARstar OPTIMA plate reader (BMG Labtechnologies, Germany). Experiments were performed in triplicates and GI_{50} values were calculated using the Graphpad Prism software. GI_{50} was defined as the concentration that led to 50% viable cells.

Detection of α-tubulin acetylation levels by immunofluorescence. PC-3M-luc cells (20,000 cells per well) were plated in ibidi 8-well µ-slides (ibidi, cat. #80826) and incubated overnight at 37 °C, 5% CO_2. After treatment with 20 µM of inhibitors for 6 hours, medium was removed, cells were washed with PBS and fixed with 4% PFA for 8-10 min at room temperature. Cells were rinsed three times with PBS and lysed with extraction buffer (PBS, 0.1% Triton X-100) for 3-5 min at room temperature, followed by another washing step with PBS. After the addition of blocking buffer (PBS, 0.1% Triton, 2-5% FCS), acetyl-α-Tubulin (Lys40) (D20G3) XP Rabbit mAb Alexa Fluor 647 Conjugate (1:50, #81502) was added overnight at 4 °C in the dark. The cells were rinsed again two times with blocking buffer and once with PBS, followed by the addition of DAPI in mounting medium (VECTASHIELD HardSet Antifade Mounting Medium with DAPI, #H-1500-10), diluted 1:50 in PBS, for at least 10 min in the dark. Confocal microscopy was performed with a Leica SP8 confocal microscope equipped with a 40_/1.40 oil objective (Leica Microsystems). The laser settings of the images were maintained constant to allow a direct comparison of signal intensities between images.

Migration assay. PC-3M-luc cells were starved overnight in RPMI-1640 Medium without FCS. Cell migration was monitored using the xCelligence system (Roche, Basel, Switzerland) that measures electrode impedance upon cell attachment to the surface of CIM-plate chambers. PC-3M-luc cells were seeded with a number of 5 x 10^4 cells into the transwell chamber containing 0% FCS RPMI 1640 in the upper chamber and 10% FCS RPMI 1640 in the lower chamber. Before starting the experiment, inhibitors were added at 20 or 10 µM to the cells in the upper chamber. The negative control was performed with 0%FCS RPMI 1640 in both chambers. Cell indices were automatically recorded every 15minutes for 72 h by the xCelligence system software (Roche). Relative velocities represent the change of the cell index over time.

ASSOCIATED CONTENT

Supporting Information

Supplementary figures and tables, HPLC data and NMR spectra are reported in the Supporting Information (link PDF)

Crystal structure in complex with 16 (link PDB)

Molecular formula strings for synthesized compounds (link CSV)

Data Availability

Atomic coordinates and structure factors for the Sirt2-**16** complex have been deposited in the Protein Data Bank (www.rcsb.org) with accession code 8PY3.

AUTHOR INFORMATION

Corresponding Author

Manfred Jung - *Institute of Pharmaceutical Sciences, University of Freiburg, Albertstraße 25, 79104 Freiburg, Germany, CIBSS – Centre for Integrative Biological Signalling Studies, University of Freiburg, Germany*; https://orcid.org/ 0000-0002-6361-7716; Phone: +49 761 203-4896 ; Email: manfred.jung@pharmazie.uni-freiburg.de

Authors

Arianna Colcerasa – *Institute of Pharmaceutical Sciences, University of Freiburg, Albertstraße 25, 79104 Freiburg, Germany*

Patrick Moser- – *Institute of Pharmaceutical Sciences, University of Freiburg, Albertstraße 25, 79104 Freiburg, Germany*

Anja Vogelmann - – *Institute of Pharmaceutical Sciences, University of Freiburg, Albertstraße 25, 79104 Freiburg, Germany*

Florian Friedrich - – *Institute of Pharmaceutical Sciences, University of Freiburg, Albertstraße 25, 79104 Freiburg, Germany*

Jelena Melesina - *Department of Medicinal Chemistry, Institute of Pharmacy, University of Halle-Wittenberg, Halle, Germany*

Emilia Neuwirt - *Institute of Neuropathology, Medical Center – University of Freiburg, Faculty of Medicine, University of Freiburg, 79106 Freiburg, Germany*

Manuela Sum - *Department of Urology and Center for Clinical Research, University of Freiburg Medical Center, 79106 Freiburg, Germany*

Lin Zhang - *Institute of Biochemistry, University of Freiburg, Albertstraße 21, 79104 Freiburg, Germany*

Elizabeth Ramos-Morales - *IGBMC, 1 rue Laurent Fries, 67400 Illkirch-Graffenstaden, France*

Christophe Romier - *IGBMC, 1 rue Laurent Fries, 67400 Illkirch-Graffenstaden, France*

Oliver Einsle - *Institute of Biochemistry, University of Freiburg, Albertstraße 21, 79104 Freiburg, Germany*

Eric Metzger - *Department of Urology and Center for Clinical Research, University of Freiburg Medical Center, 79106 Freiburg, Germany*

Roland Schüle - *Department of Urology and Center for Clinical Research, University of Freiburg Medical Center, 79106 Freiburg, Germany*

Olaf Groß- *Institute of Neuropathology, Medical Center – University of Freiburg, Faculty of Medicine, University of Freiburg, 79106 Freiburg, Germany*

Wolfgang Sippl - *Department of Medicinal Chemistry, Institute of Pharmacy, University of Halle-Wittenberg, Halle, Germany*

Author Contributions

A.C., P.M. and P. T. performed the chemical synthesis, A.C. carried out the biochemical characterization; docking studies were conducted by J.M; F.F carried out X-ray crystallographic studies; A.V, E.N. and M.S. performed cell-based assays, F.F, L.Z. and E.R-M. expressed and purified proteins under investigation. A.C. and M.J. wrote the original draft of the manuscript; all authors have given approval to the final manuscript. The study was conducted under the supervision of C.R, O.E, E.M., R.S, O.G, W.S. and M.J.

Notes

There are no conflicts to declare.

ACKNOWLEDGEMENTS

This research utilized the beamline ID30A-3 (MASSIF-3) at the European Synchrotron Radiation Facility (ESRF, Grenoble, France). This work was supported by the Deutsche Forschungsgemeinschaft (DFG, German Research Foundation) through SFB 992 (Project ID 192904750), Ju295/14-1, Si868/27-1 (Project ID 503267011), GRK1976 (Project ID 235777276), SFB 1160 (Project ID 256073931), SFB/TRR 167 (Project ID 259373024), SFB 1425 (Project ID 422681845), SFB 1479 (Project ID 441891347), GRK 2606 (Project ID 423813989). We thank the Germany's Excellence Strategy (CIBSS - EXC-2189 - Project ID 390939984), as well as the European Research Council (ERC) through Starting Grant 337689 and Proof-of-Concept Grant 966687 (to OG). C.R. and E.R-M. were supported by institutional funds from the Centre National de la Recherche Scientifique (CNRS), the Institut National de la Santé et de la Recherche Médicale (INSERM) and the Université de Strasbourg.

ABBREVIATIONS

AMC, 7-Amino-4-methylcoumarin; CD, Circular Dichroism; DSF, Differential Scanning Fluorimety; FP, Fluorescence Polarization; HDAC, Histone deacetylase; Hela, Cervical cancer cells (Henrietta Lacks); HM, Homology model; IC_{50}, Half maximal inhibitory concentration; NAD^+, Nicotinamide adenine dinucleotide; PC-3M-luc, Metastatic prostate cancer luciferase cells; *Sm, Schistosoma mansoni;* Sirt, Sirtuin; ZMAL, Z-(Ac) Lys-AMC; ZMML, Z-(Myr) Lys-AMC

REFERENCES

(1) Imai, S.; Armstrong, C. M.; Kaeberlein, M.; Guarente, L. Transcriptional Silencing and Longevity Protein Sir2 Is an NAD-Dependent Histone Deacetylase. *Nature* **2000**, *403* (6771), 795–800. https://doi.org/10.1038/35001622.

(2) de Ruijter, A. J. M.; van Gennip, A. H.; Caron, H. N.; Kemp, S.; van Kuilenburg, A. B. P. Histone Deacetylases (HDACs): Characterization of the Classical HDAC Family. *Biochem J* **2003**, *370* (Pt 3), 737–749. https://doi.org/10.1042/BJ20021321.
(3) Finnin, M. S.; Donigian, J. R.; Pavletich, N. P. Structure of the Histone Deacetylase SIRT2. *Nat Struct Biol* **2001**, *8* (7), 621–625. https://doi.org/10.1038/89668.
(4) Moniot, S.; Schutkowski, M.; Steegborn, C. Crystal Structure Analysis of Human Sirt2 and Its ADP-Ribose Complex. *J Struct Biol* **2013**, *182* (2), 136–143. https://doi.org/10.1016/j.jsb.2013.02.012.
(5) Schiedel, M.; Robaa, D.; Rumpf, T.; Sippl, W.; Jung, M. The Current State of NAD+-Dependent Histone Deacetylases (Sirtuins) as Novel Therapeutic Targets. *Medicinal Research Reviews* **2018**, *38* (1), 147–200. https://doi.org/10.1002/med.21436.
(6) Michishita, E.; Park, J. Y.; Burneskis, J. M.; Barrett, J. C.; Horikawa, I. Evolutionarily Conserved and Nonconserved Cellular Localizations and Functions of Human SIRT Proteins. *Mol Biol Cell* **2005**, *16* (10), 4623–4635. https://doi.org/10.1091/mbc.e05-01-0033.
(7) Tanno, M.; Sakamoto, J.; Miura, T.; Shimamoto, K.; Horio, Y. Nucleocytoplasmic Shuttling of the NAD+-Dependent Histone Deacetylase SIRT1. *J Biol Chem* **2007**, *282* (9), 6823–6832. https://doi.org/10.1074/jbc.M609554200.
(8) Lombard, D. B.; Alt, F. W.; Cheng, H.-L.; Bunkenborg, J.; Streeper, R. S.; Mostoslavsky, R.; Kim, J.; Yancopoulos, G.; Valenzuela, D.; Murphy, A.; Yang, Y.; Chen, Y.; Hirschey, M. D.; Bronson, R. T.; Haigis, M.; Guarente, L. P.; Farese, R. V.; Weissman, S.; Verdin, E.; Schwer, B. Mammalian Sir2 Homolog SIRT3 Regulates Global Mitochondrial Lysine Acetylation. *Mol Cell Biol* **2007**, *27* (24), 8807–8814. https://doi.org/10.1128/MCB.01636-07.
(9) Feldman, J. L.; Baeza, J.; Denu, J. M. Activation of the Protein Deacetylase SIRT6 by Long-Chain Fatty Acids and Widespread Deacylation by Mammalian Sirtuins*. *Journal of Biological Chemistry* **2013**, *288* (43), 31350–31356. https://doi.org/10.1074/jbc.C113.511261.
(10) Jiang, H.; Khan, S.; Wang, Y.; Charron, G.; He, B.; Sebastian, C.; Du, J.; Kim, R.; Ge, E.; Mostoslavsky, R.; Hang, H. C.; Hao, Q.; Lin, H. SIRT6 Regulates TNF-α Secretion through Hydrolysis of Long-Chain Fatty Acyl Lysine. *Nature* **2013**, *496* (7443), 110–113. https://doi.org/10.1038/nature12038.
(11) Zhang, X.; Spiegelman, N. A.; Nelson, O. D.; Jing, H.; Lin, H. SIRT6 Regulates Ras-Related Protein R-Ras2 by Lysine Defatty-Acylation. *eLife* **2017**, *6*, e25158. https://doi.org/10.7554/eLife.25158.
(12) Tan, M.; Peng, C.; Anderson, K. A.; Chhoy, P.; Xie, Z.; Dai, L.; Park, J.; Chen, Y.; Huang, H.; Zhang, Y.; Ro, J.; Wagner, G. R.; Green, M. F.; Madsen, A. S.; Schmiesing, J.; Peterson, B. S.; Xu, G.; Ilkayeva, O. R.; Muehlbauer, M. J.; Braulke, T.; Mühlhausen, C.; Backos, D. S.; Olsen, C. A.; McGuire, P. J.; Pletcher, S. D.; Lombard, D. B.; Hirschey, M. D.; Zhao, Y. Lysine Glutarylation Is a Protein Posttranslational Modification Regulated by SIRT5. *Cell Metab* **2014**, *19* (4), 605–617. https://doi.org/10.1016/j.cmet.2014.03.014.
(13) Du, J.; Zhou, Y.; Su, X.; Yu, J. J.; Khan, S.; Jiang, H.; Kim, J.; Woo, J.; Kim, J. H.; Choi, B. H.; He, B.; Chen, W.; Zhang, S.; Cerione, R. A.; Auwerx, J.; Hao, Q.; Lin, H. Sirt5 Is a NAD-Dependent Protein Lysine Demalonylase and Desuccinylase. *Science* **2011**, *334* (6057), 806–809. https://doi.org/10.1126/science.1207861.
(14) Vaquero, A.; Scher, M.; Lee, D.; Erdjument-Bromage, H.; Tempst, P.; Reinberg, D. Human SirT1 Interacts with Histone H1 and Promotes Formation of Facultative Heterochromatin. *Mol Cell* **2004**, *16* (1), 93–105. https://doi.org/10.1016/j.molcel.2004.08.031.
(15) Vaziri, H.; Dessain, S. K.; Ng Eaton, E.; Imai, S. I.; Frye, R. A.; Pandita, T. K.; Guarente, L.; Weinberg, R. A. HSIR2(SIRT1) Functions as an NAD-Dependent P53 Deacetylase. *Cell* **2001**, *107* (2), 149–159. https://doi.org/10.1016/s0092-8674(01)00527-x.
(16) Tseng, A. H. H.; Shieh, S.-S.; Wang, D. L. SIRT3 Deacetylates FOXO3 to Protect Mitochondria against Oxidative Damage. *Free Radic Biol Med* **2013**, *63*, 222–234. https://doi.org/10.1016/j.freeradbiomed.2013.05.002.

(17) Bao, X.; Wang, Y.; Li, X.; Li, X.-M.; Liu, Z.; Yang, T.; Wong, C. F.; Zhang, J.; Hao, Q.; Li, X. D. Identification of "erasers" for Lysine Crotonylated Histone Marks Using a Chemical Proteomics Approach. *Elife* **2014**, *3*. https://doi.org/10.7554/eLife.02999.
(18) North, B. J.; Verdin, E. Interphase Nucleo-Cytoplasmic Shuttling and Localization of SIRT2 during Mitosis. *PLOS ONE* **2007**, *2* (8), e784. https://doi.org/10.1371/journal.pone.0000784.
(19) Vaquero, A.; Scher, M. B.; Lee, D. H.; Sutton, A.; Cheng, H.-L.; Alt, F. W.; Serrano, L.; Sternglanz, R.; Reinberg, D. SirT2 Is a Histone Deacetylase with Preference for Histone H4 Lys 16 during Mitosis. *Genes Dev* **2006**, *20* (10), 1256–1261. https://doi.org/10.1101/gad.1412706.
(20) Serrano, L.; Martínez-Redondo, P.; Marazuela-Duque, A.; Vazquez, B. N.; Dooley, S. J.; Voigt, P.; Beck, D. B.; Kane-Goldsmith, N.; Tong, Q.; Rabanal, R. M.; Fondevila, D.; Muñoz, P.; Krüger, M.; Tischfield, J. A.; Vaquero, A. The Tumor Suppressor SirT2 Regulates Cell Cycle Progression and Genome Stability by Modulating the Mitotic Deposition of H4K20 Methylation. *Genes Dev* **2013**, *27* (6), 639–653. https://doi.org/10.1101/gad.211342.112.
(21) Eskandarian, H. A.; Impens, F.; Nahori, M.-A.; Soubigou, G.; Coppée, J.-Y.; Cossart, P.; Hamon, M. A. A Role for SIRT2-Dependent Histone H3K18 Deacetylation in Bacterial Infection. *Science* **2013**, *341* (6145). https://doi.org/10.1126/science.1238858.
(22) Liu, P. Y.; Xu, N.; Malyukova, A.; Scarlett, C. J.; Sun, Y. T.; Zhang, X. D.; Ling, D.; Su, S.-P.; Nelson, C.; Chang, D. K.; Koach, J.; Tee, A. E.; Haber, M.; Norris, M. D.; Toon, C.; Rooman, I.; Xue, C.; Cheung, B. B.; Kumar, S.; Marshall, G. M.; Biankin, A. V.; Liu, T. The Histone Deacetylase SIRT2 Stabilizes Myc Oncoproteins. *Cell Death Differ* **2013**, *20* (3), 503–514. https://doi.org/10.1038/cdd.2012.147.
(23) Baker, D. J.; Dawlaty, M. M.; Wijshake, T.; Jeganathan, K. B.; Malureanu, L.; van Ree, J. H.; Crespo-Diaz, R.; Reyes, S.; Seaburg, L.; Shapiro, V.; Behfar, A.; Terzic, A.; van de Sluis, B.; van Deursen, J. M. Increased Expression of BubR1 Protects against Aneuploidy and Cancer and Extends Healthy Lifespan. *Nat Cell Biol* **2013**, *15* (1), 96–102. https://doi.org/10.1038/ncb2643.
(24) Jin, Y.-H.; Kim, Y.-J.; Kim, D.-W.; Baek, K.-H.; Kang, B. Y.; Yeo, C.-Y.; Lee, K.-Y. Sirt2 Interacts with 14-3-3 Beta/Gamma and down-Regulates the Activity of P53. *Biochem Biophys Res Commun* **2008**, *368* (3), 690–695. https://doi.org/10.1016/j.bbrc.2008.01.114.
(25) Jiang, W.; Wang, S.; Xiao, M.; Lin, Y.; Zhou, L.; Lei, Q.; Xiong, Y.; Guan, K.-L.; Zhao, S. Acetylation Regulates Gluconeogenesis by Promoting PEPCK1 Degradation via Recruiting the UBR5 Ubiquitin Ligase. *Mol Cell* **2011**, *43* (1), 33–44. https://doi.org/10.1016/j.molcel.2011.04.028.
(26) Kim, H.-S.; Vassilopoulos, A.; Wang, R.-H.; Lahusen, T.; Xiao, Z.; Xu, X.; Li, C.; Veenstra, T. D.; Li, B.; Yu, H.; Ji, J.; Wang, X. W.; Park, S.-H.; Cha, Y. I.; Gius, D.; Deng, C.-X. SIRT2 Maintains Genome Integrity and Suppresses Tumorigenesis through Regulating APC/C Activity. *Cancer Cell* **2011**, *20* (4), 487–499. https://doi.org/10.1016/j.ccr.2011.09.004.
(27) North, B. J.; Marshall, B. L.; Borra, M. T.; Denu, J. M.; Verdin, E. The Human Sir2 Ortholog, SIRT2, Is an NAD+-Dependent Tubulin Deacetylase. *Molecular Cell* **2003**, *11* (2), 437–444. https://doi.org/10.1016/S1097-2765(03)00038-8.
(28) Teng, Y.-B.; Jing, H.; Aramsangtienchai, P.; He, B.; Khan, S.; Hu, J.; Lin, H.; Hao, Q. Efficient Demyristoylase Activity of SIRT2 Revealed by Kinetic and Structural Studies. *Sci Rep* **2015**, *5* (1), 8529. https://doi.org/10.1038/srep08529.
(29) Feldman, J. L.; Dittenhafer-Reed, K. E.; Kudo, N.; Thelen, J. N.; Ito, A.; Yoshida, M.; Denu, J. M. Kinetic and Structural Basis for Acyl-Group Selectivity and NAD $^{+}$ Dependence in Sirtuin-Catalyzed Deacylation. *Biochemistry* **2015**, *54* (19), 3037–3050. https://doi.org/10.1021/acs.biochem.5b00150.
(30) Swyter, S.; Schiedel, M.; Monaldi, D.; Szunyogh, S.; Lehotzky, A.; Rumpf, T.; Ovádi, J.; Sippl, W.; Jung, M. New Chemical Tools for Probing Activity and Inhibition of the NAD+-Dependent Lysine Deacylase Sirtuin 2. *Philosophical Transactions of the Royal Society B: Biological Sciences* **2018**, *373* (1748), 20170083. https://doi.org/10.1098/rstb.2017.0083.

(31) Galleano, I.; Schiedel, M.; Jung, M.; Madsen, A. S.; Olsen, C. A. A Continuous, Fluorogenic Sirtuin 2 Deacylase Assay: Substrate Screening and Inhibitor Evaluation. *J. Med. Chem.* **2016**, *59* (3), 1021–1031. https://doi.org/10.1021/acs.jmedchem.5b01532.
(32) Vogelmann, A.; Schiedel, M.; Wössner, N.; Merz, A.; Herp, D.; Hammelmann, S.; Colcerasa, A.; Komaniecki, G.; Hong, J.; Sum, M.; Metzger, E.; Neuwirt, E.; Zhang, L.; Einsle, O.; Groß, O.; Schüle, R.; Lin, H.; Sippl, W.; Jung, M. Development of a NanoBRET Assay to Validate Inhibitors of Sirt2-Mediated Lysine Deacetylation and Defatty-Acylation That Block Prostate Cancer Cell Migration. *RSC Chem. Biol.* **2022**, *3* (4), 468–485. https://doi.org/10.1039/D1CB00244A.
(33) Jing, H.; Zhang, X.; Wisner, S. A.; Chen, X.; Spiegelman, N. A.; Linder, M. E.; Lin, H. SIRT2 and Lysine Fatty Acylation Regulate the Transforming Activity of K-Ras4a. *eLife* **2017**, *6*, e32436. https://doi.org/10.7554/eLife.32436.
(34) Spiegelman, N. A.; Zhang, X.; Jing, H.; Cao, J.; Kotliar, I. B.; Aramsangtienchai, P.; Wang, M.; Tong, Z.; Rosch, K. M.; Lin, H. SIRT2 and Lysine Fatty Acylation Regulate the Activity of RalB and Cell Migration. *ACS Chem. Biol.* **2019**, *14* (9), 2014–2023. https://doi.org/10.1021/acschembio.9b00492.
(35) Kosciuk, T.; Price, I. R.; Zhang, X.; Zhu, C.; Johnson, K. N.; Zhang, S.; Halaby, S. L.; Komaniecki, G. P.; Yang, M.; DeHart, C. J.; Thomas, P. M.; Kelleher, N. L.; Fromme, J. C.; Lin, H. NMT1 and NMT2 Are Lysine Myristoyltransferases Regulating the ARF6 GTPase Cycle. *Nat Commun* **2020**, *11* (1), 1067. https://doi.org/10.1038/s41467-020-14893-x.
(36) Jing, H.; Hu, J.; He, B.; Negrón Abril, Y. L.; Stupinski, J.; Weiser, K.; Carbonaro, M.; Chiang, Y.-L.; Southard, T.; Giannakakou, P.; Weiss, R. S.; Lin, H. A SIRT2-Selective Inhibitor Promotes c-Myc Oncoprotein Degradation and Exhibits Broad Anticancer Activity. *Cancer Cell* **2016**, *29* (3), 297–310. https://doi.org/10.1016/j.ccell.2016.02.007.
(37) Spiegelman, N. A.; Hong, J. Y.; Hu, J.; Jing, H.; Wang, M.; Price, I. R.; Cao, J.; Yang, M.; Zhang, X.; Lin, H. A Small-Molecule SIRT2 Inhibitor That Promotes K-Ras4a Lysine Fatty-Acylation. *ChemMedChem* **2019**, *14* (7), 744–748. https://doi.org/10.1002/cmdc.201800715.
(38) Nielsen, A. L.; Rajabi, N.; Kudo, N.; Lundø, K.; Moreno-Yruela, C.; Bæk, M.; Fontenas, M.; Lucidi, A.; Madsen, A. S.; Yoshida, M.; Olsen, C. A. Mechanism-Based Inhibitors of SIRT2: Structure–Activity Relationship, X-Ray Structures, Target Engagement, Regulation of α-Tubulin Acetylation and Inhibition of Breast Cancer Cell Migration. *RSC Chem. Biol.* **2021**, *2* (2), 612–626. https://doi.org/10.1039/D0CB00036A.
(39) Vogelmann, A.; Schiedel, M.; Wössner, N.; Merz, A.; Herp, D.; Hammelmann, S.; Colcerasa, A.; Komaniecki, G.; Hong, J.; Sum, M.; Metzger, E.; Neuwirt, E.; Zhang, L.; Einsle, O.; Groß, O.; Schüle, R.; Lin, H.; Sippl, W.; Jung, M. Development of a NanoBRET Assay to Validate Inhibitors of Sirt2-Mediated Lysine Deacetylation and Defatty-Acylation That Block Prostate Cancer Cell Migration. *RSC Chem. Biol.* **2022**, *3* (4), 468–485. https://doi.org/10.1039/D1CB00244A.
(40) Hong, J. Y.; Fernandez, I.; Anmangandla, A.; Lu, X.; Bai, J. J.; Lin, H. Pharmacological Advantage of SIRT2-Selective versus Pan-SIRT1-3 Inhibitors. *ACS Chem Biol* **2021**, *16* (7), 1266–1275. https://doi.org/10.1021/acschembio.1c00331.
(41) North, B. J.; Rosenberg, M. A.; Jeganathan, K. B.; Hafner, A. V.; Michan, S.; Dai, J.; Baker, D. J.; Cen, Y.; Wu, L. E.; Sauve, A. A.; Deursen, J. M. van; Rosenzweig, A.; Sinclair, D. A. SIRT2 Induces the Checkpoint Kinase BubR1 to Increase Lifespan. *The EMBO Journal* **2014**, *33* (13), 1438–1453. https://doi.org/10.15252/embj.201386907.
(42) Liu, Y.; Zhang, Y.; Zhu, K.; Chi, S.; Wang, C.; Xie, A. Emerging Role of Sirtuin 2 in Parkinson's Disease. *Front Aging Neurosci* **2019**, *11*, 372. https://doi.org/10.3389/fnagi.2019.00372.
(43) Chen, G.; Huang, P.; Hu, C. The Role of SIRT2 in Cancer: A Novel Therapeutic Target. *International Journal of Cancer* **2020**, *147* (12), 3297–3304. https://doi.org/10.1002/ijc.33118.

(44) Wang, Y.; Yang, J.; Hong, T.; Chen, X.; Cui, L. SIRT2: Controversy and Multiple Roles in Disease and Physiology. *Ageing Res Rev* **2019**, *55*, 100961. https://doi.org/10.1016/j.arr.2019.100961.
(45) Zhang, L.; Kim, S.; Ren, X. The Clinical Significance of SIRT2 in Malignancies: A Tumor Suppressor or an Oncogene? *Front. Oncol.* **2020**, *10*. https://doi.org/10.3389/fonc.2020.01721.
(46) Jing, H.; Hu, J.; He, B.; Negrón Abril, Y. L.; Stupinski, J.; Weiser, K.; Carbonaro, M.; Chiang, Y.-L.; Southard, T.; Giannakakou, P.; Weiss, R. S.; Lin, H. A SIRT2-Selective Inhibitor Promotes c-Myc Oncoprotein Degradation and Exhibits Broad Anticancer Activity. *Cancer Cell* **2016**, *29* (3), 297–310. https://doi.org/10.1016/j.ccell.2016.02.007.
(47) Spiegelman, N. A.; Hong, J. Y.; Hu, J.; Jing, H.; Wang, M.; Price, I. R.; Cao, J.; Yang, M.; Zhang, X.; Lin, H. A Small-Molecule SIRT2 Inhibitor That Promotes K-Ras4a Lysine Fatty-Acylation. *ChemMedChem* **2019**, *14* (7), 744–748. https://doi.org/10.1002/cmdc.201800715.
(48) Nielsen, A. L.; Rajabi, N.; Kudo, N.; Lundø, K.; Moreno-Yruela, C.; Bæk, M.; Fontenas, M.; Lucidi, A.; Madsen, A. S.; Yoshida, M.; Olsen, C. A. Mechanism-Based Inhibitors of SIRT2: Structure–Activity Relationship, X-Ray Structures, Target Engagement, Regulation of α-Tubulin Acetylation and Inhibition of Breast Cancer Cell Migration. *RSC Chem. Biol.* **2021**, *2* (2), 612–626. https://doi.org/10.1039/D0CB00036A.
(49) Fioravanti, R.; Mautone, N.; Rovere, A.; Rotili, D.; Mai, A. Targeting Histone Acetylation/Deacetylation in Parasites: An Update (2017-2020). *Curr Opin Chem Biol* **2020**, *57*, 65–74. https://doi.org/10.1016/j.cbpa.2020.05.008.
(50) Pierce, R. J.; Dubois-Abdesselem, F.; Lancelot, J.; Andrade, L.; Oliveira, G. Targeting Schistosome Histone Modifying Enzymes for Drug Development. *Curr Pharm Des* **2012**, *18* (24), 3567–3578.
(51) Carneiro, V. C.; Silva, I. C. de A. da; Torres, E. J. L.; Caby, S.; Lancelot, J.; Vanderstraete, M.; Furdas, S. D.; Jung, M.; Pierce, R. J.; Fantappié, M. R. Epigenetic Changes Modulate Schistosome Egg Formation and Are a Novel Target for Reducing Transmission of Schistosomiasis. *PLOS Pathogens* **2014**, *10* (5), e1004116. https://doi.org/10.1371/journal.ppat.1004116.
(52) Cabezas-Cruz, A.; Lancelot, J.; Caby, S.; Oliveira, G.; Pierce, R. J. Epigenetic Control of Gene Function in Schistosomes: A Source of Therapeutic Targets? *Front Genet* **2014**, *5*, 317. https://doi.org/10.3389/fgene.2014.00317.
(53) Lancelot, J.; Caby, S.; Dubois-Abdesselem, F.; Vanderstraete, M.; Trolet, J.; Oliveira, G.; Bracher, F.; Jung, M.; Pierce, R. J. Schistosoma Mansoni Sirtuins: Characterization and Potential as Chemotherapeutic Targets. *PLOS Neglected Tropical Diseases* **2013**, *7* (9), e2428. https://doi.org/10.1371/journal.pntd.0002428.
(54) Hailu, G. S.; Robaa, D.; Forgione, M.; Sippl, W.; Rotili, D.; Mai, A. Lysine Deacetylase Inhibitors in Parasites: Past, Present, and Future Perspectives. *J Med Chem* **2017**, *60* (12), 4780–4804. https://doi.org/10.1021/acs.jmedchem.6b01595.
(55) Marek, M.; Oliveira, G.; Pierce, R. J.; Jung, M.; Sippl, W.; Romier, C. Drugging the Schistosome Zinc-Dependent HDACs: Current Progress and Future Perspectives. *Future Med Chem* **2015**, *7* (6), 783–800. https://doi.org/10.4155/fmc.15.25.
(56) Oliveira, G. Cancer and Parasitic Infections: Similarities and Opportunities for the Development of New Control Tools. *Rev Soc Bras Med Trop* **2014**, *47* (1), 1–2. https://doi.org/10.1590/0037-8682-0013-2014.
(57) Martinez-Outschoorn, U. E.; Pestell, R. G.; Howell, A.; Tykocinski, M. L.; Nagajyothi, F.; Machado, F. S.; Tanowitz, H. B.; Sotgia, F.; Lisanti, M. P. Energy Transfer in "Parasitic" Cancer Metabolism: Mitochondria Are the Powerhouse and Achilles' Heel of Tumor Cells. *Cell Cycle* **2011**, *10* (24), 4208–4216. https://doi.org/10.4161/cc.10.24.18487.
(58) Kaelin, W. G.; McKnight, S. L. Influence of Metabolism on Epigenetics and Disease. *Cell* **2013**, *153* (1), 56–69. https://doi.org/10.1016/j.cell.2013.03.004.

(59) Thompson, D. P.; Morrison, D. D.; Pax, R. A.; Bennett, J. L. Changes in Glucose Metabolism and Cyanide Sensitivity in Schistosoma Mansoni during Development. *Mol Biochem Parasitol* **1984**, *13* (1), 39–51. https://doi.org/10.1016/0166-6851(84)90100-2.
(60) Koppenol, W. H.; Bounds, P. L.; Dang, C. V. Otto Warburg's Contributions to Current Concepts of Cancer Metabolism. *Nat Rev Cancer* **2011**, *11* (5), 325–337. https://doi.org/10.1038/nrc3038.
(61) Andrews, K. T.; Fisher, G.; Skinner-Adams, T. S. Drug Repurposing and Human Parasitic Protozoan Diseases. *Int J Parasitol Drugs Drug Resist* **2014**, *4* (2), 95–111. https://doi.org/10.1016/j.ijpddr.2014.02.002.
(62) Dissous, C.; Grevelding, C. G. Piggy-Backing the Concept of Cancer Drugs for Schistosomiasis Treatment: A Tangible Perspective? *Trends Parasitol* **2011**, *27* (2), 59–66. https://doi.org/10.1016/j.pt.2010.09.001.
(63) Marek, M.; Kannan, S.; Hauser, A.-T.; Moraes Mourão, M.; Caby, S.; Cura, V.; Stolfa, D. A.; Schmidtkunz, K.; Lancelot, J.; Andrade, L.; Renaud, J.-P.; Oliveira, G.; Sippl, W.; Jung, M.; Cavarelli, J.; Pierce, R. J.; Romier, C. Structural Basis for the Inhibition of Histone Deacetylase 8 (HDAC8), a Key Epigenetic Player in the Blood Fluke Schistosoma Mansoni. *PLoS Pathog* **2013**, *9* (9), e1003645. https://doi.org/10.1371/journal.ppat.1003645.
(64) Heimburg, T.; Chakrabarti, A.; Lancelot, J.; Marek, M.; Melesina, J.; Hauser, A.-T.; Shaik, T. B.; Duclaud, S.; Robaa, D.; Erdmann, F.; Schmidt, M.; Romier, C.; Pierce, R. J.; Jung, M.; Sippl, W. Structure-Based Design and Synthesis of Novel Inhibitors Targeting HDAC8 from Schistosoma Mansoni for the Treatment of Schistosomiasis. *J. Med. Chem.* **2016**, *59* (6), 2423–2435. https://doi.org/10.1021/acs.jmedchem.5b01478.
(65) Kannan, S.; Melesina, J.; Hauser, A.-T.; Chakrabarti, A.; Heimburg, T.; Schmidtkunz, K.; Walter, A.; Marek, M.; Pierce, R. J.; Romier, C.; Jung, M.; Sippl, W. Discovery of Inhibitors of Schistosoma Mansoni HDAC8 by Combining Homology Modeling, Virtual Screening, and in Vitro Validation. *J Chem Inf Model* **2014**, *54* (10), 3005–3019. https://doi.org/10.1021/ci5004653.
(66) Stolfa, D. A.; Marek, M.; Lancelot, J.; Hauser, A.-T.; Walter, A.; Leproult, E.; Melesina, J.; Rumpf, T.; Wurtz, J.-M.; Cavarelli, J.; Sippl, W.; Pierce, R. J.; Romier, C.; Jung, M. Molecular Basis for the Antiparasitic Activity of a Mercaptoacetamide Derivative That Inhibits Histone Deacetylase 8 (HDAC8) from the Human Pathogen Schistosoma Mansoni. *J Mol Biol* **2014**, *426* (20), 3442–3453. https://doi.org/10.1016/j.jmb.2014.03.007.
(67) Lancelot, J.; Caby, S.; Dubois-Abdesselem, F.; Vanderstraete, M.; Trolet, J.; Oliveira, G.; Bracher, F.; Jung, M.; Pierce, R. J. Schistosoma Mansoni Sirtuins: Characterization and Potential as Chemotherapeutic Targets. *PLOS Neglected Tropical Diseases* **2013**, *7* (9), e2428. https://doi.org/10.1371/journal.pntd.0002428.
(68) Monaldi, D.; Rotili, D.; Lancelot, J.; Marek, M.; Wössner, N.; Lucidi, A.; Tomaselli, D.; Ramos-Morales, E.; Romier, C.; Pierce, R. J.; Mai, A.; Jung, M. Structure–Reactivity Relationships on Substrates and Inhibitors of the Lysine Deacylase Sirtuin 2 from Schistosoma Mansoni (SmSirt2). *J. Med. Chem.* **2019**, *62* (19), 8733–8759. https://doi.org/10.1021/acs.jmedchem.9b00638.
(69) Peña, I.; Pilar Manzano, M.; Cantizani, J.; Kessler, A.; Alonso-Padilla, J.; Bardera, A. I.; Alvarez, E.; Colmenarejo, G.; Cotillo, I.; Roquero, I.; de Dios-Anton, F.; Barroso, V.; Rodriguez, A.; Gray, D. W.; Navarro, M.; Kumar, V.; Sherstnev, A.; Drewry, D. H.; Brown, J. R.; Fiandor, J. M.; Julio Martin, J. New Compound Sets Identified from High Throughput Phenotypic Screening Against Three Kinetoplastid Parasites: An Open Resource. *Scientific Reports* **2015**, *5* (1), 8771. https://doi.org/10.1038/srep08771.
(70) Schiedel, M.; Rumpf, T.; Karaman, B.; Lehotzky, A.; Gerhardt, S.; Ovádi, J.; Sippl, W.; Einsle, O.; Jung, M. Structure-Based Development of an Affinity Probe for Sirtuin 2. *Angewandte Chemie International Edition* **2016**, *55* (6), 2252–2256. https://doi.org/10.1002/anie.201509843.

(71) Schiedel, M.; Marek, M.; Lancelot, J.; Karaman, B.; Almlöf, I.; Schultz, J.; Sippl, W.; Pierce, R. J.; Romier, C.; Jung, M. Fluorescence-Based Screening Assays for the NAD+-Dependent Histone Deacetylase SmSirt2 from Schistosoma Mansoni. *J Biomol Screen* **2015**, *20* (1), 112–121. https://doi.org/10.1177/1087057114555307.
(72) Baykov, S.; Sharonova, T.; Shetnev, A.; Rozhkov, S.; Kalinin, S.; Smirnov, A. V. The First One-Pot Ambient-Temperature Synthesis of 1,2,4-Oxadiazoles from Amidoximes and Carboxylic Acid Esters. *Tetrahedron* **2017**, *7* (73), 945–951. https://doi.org/10.1016/j.tet.2017.01.007.
(73) Heltweg, B.; Jung, M. A Homogeneous Nonisotopic Histone Deacetylase Activity Assay. *J Biomol Screen* **2003**, *8* (1), 89–95. https://doi.org/10.1177/1087057102239644.
(74) Rumpf, T.; Schiedel, M.; Karaman, B.; Roessler, C.; North, B. J.; Lehotzky, A.; Oláh, J.; Ladwein, K. I.; Schmidtkunz, K.; Gajer, M.; Pannek, M.; Steegborn, C.; Sinclair, D. A.; Gerhardt, S.; Ovádi, J.; Schutkowski, M.; Sippl, W.; Einsle, O.; Jung, M. Selective Sirt2 Inhibition by Ligand-Induced Rearrangement of the Active Site. *Nature Communications* **2015**, *6* (1), 6263. https://doi.org/10.1038/ncomms7263.
(75) Swyter, S.; Schiedel, M.; Monaldi, D.; Szunyogh, S.; Lehotzky, A.; Rumpf, T.; Ovádi, J.; Sippl, W.; Jung, M. New Chemical Tools for Probing Activity and Inhibition of the NAD+-Dependent Lysine Deacylase Sirtuin 2. *Philosophical Transactions of the Royal Society B: Biological Sciences* **2018**, *373* (1748), 20170083. https://doi.org/10.1098/rstb.2017.0083.
(76) North, B. J.; Marshall, B. L.; Borra, M. T.; Denu, J. M.; Verdin, E. The Human Sir2 Ortholog, SIRT2, Is an NAD+-Dependent Tubulin Deacetylase. *Mol Cell* **2003**, *11* (2), 437–444. https://doi.org/10.1016/s1097-2765(03)00038-8.
(77) Monaldi, D.; Rotili, D.; Lancelot, J.; Marek, M.; Wössner, N.; Lucidi, A.; Tomaselli, D.; Ramos-Morales, E.; Romier, C.; Pierce, R. J.; Mai, A.; Jung, M. Structure–Reactivity Relationships on Substrates and Inhibitors of the Lysine Deacylase Sirtuin 2 from *Schistosoma Mansoni* (*Sm* Sirt2). *J. Med. Chem.* **2019**, *62* (19), 8733–8759. https://doi.org/10.1021/acs.jmedchem.9b00638.
(78) Berman, H. M.; Westbrook, J.; Feng, Z.; Gilliland, G.; Bhat, T. N.; Weissig, H.; Shindyalov, I. N.; Bourne, P. E. The Protein Data Bank. *Nucleic Acids Research* **2000**, *28* (1), 235–242. https://doi.org/10.1093/nar/28.1.235.
(79) Waterhouse, A.; Bertoni, M.; Bienert, S.; Studer, G.; Tauriello, G.; Gumienny, R.; Heer, F. T.; de Beer, T. A. P.; Rempfer, C.; Bordoli, L.; Lepore, R.; Schwede, T. SWISS-MODEL: Homology Modelling of Protein Structures and Complexes. *Nucleic Acids Research* **2018**, *46* (W1), W296–W303. https://doi.org/10.1093/nar/gky427.
(80) Harder, E.; Damm, W.; Maple, J.; Wu, C.; Reboul, M.; Xiang, J. Y.; Wang, L.; Lupyan, D.; Dahlgren, M. K.; Knight, J. L.; Kaus, J. W.; Cerutti, D. S.; Krilov, G.; Jorgensen, W. L.; Abel, R.; Friesner, R. A. OPLS3: A Force Field Providing Broad Coverage of Drug-like Small Molecules and Proteins. *J. Chem. Theory Comput.* **2016**, *12* (1), 281–296. https://doi.org/10.1021/acs.jctc.5b00864.
(81) *Development of First-in-Class Dual Sirt2/HDAC6 Inhibitors as Molecular Tools for Dual Inhibition of Tubulin Deacetylation | Journal of Medicinal Chemistry*. https://pubs.acs.org/doi/full/10.1021/acs.jmedchem.3c01385 (accessed 2023-11-16).
(82) Vonrhein, C.; Flensburg, C.; Keller, P.; Sharff, A.; Smart, O.; Paciorek, W.; Womack, T.; Bricogne, G. Data Processing and Analysis with the *AutoPROC* Toolbox. *Acta Crystallogr D Biol Crystallogr* **2011**, *67* (4), 293–302. https://doi.org/10.1107/S0907444911007773.
(83) Winn, M. D.; Ballard, C. C.; Cowtan, K. D.; Dodson, E. J.; Emsley, P.; Evans, P. R.; Keegan, R. M.; Krissinel, E. B.; Leslie, A. G. W.; McCoy, A.; McNicholas, S. J.; Murshudov, G. N.; Pannu, N. S.; Potterton, E. A.; Powell, H. R.; Read, R. J.; Vagin, A.; Wilson, K. S. Overview of the CCP4 Suite and Current Developments. *Acta Cryst D* **2011**, *67* (4), 235–242. https://doi.org/10.1107/S0907444910045749.

(84) McCoy, A. J.; Grosse-Kunstleve, R. W.; Adams, P. D.; Winn, M. D.; Storoni, L. C.; Read, R. J. Phaser Crystallographic Software. *J Appl Cryst* **2007**, *40* (4), 658–674. https://doi.org/10.1107/S0021889807021206.
(85) Emsley, P.; Lohkamp, B.; Scott, W. G.; Cowtan, K. Features and Development of Coot. *Acta Cryst D* **2010**, *66* (4), 486–501. https://doi.org/10.1107/S0907444910007493.
(86) Murshudov, G. N.; Skubák, P.; Lebedev, A. A.; Pannu, N. S.; Steiner, R. A.; Nicholls, R. A.; Winn, M. D.; Long, F.; Vagin, A. A. REFMAC5 for the Refinement of Macromolecular Crystal Structures. *Acta Cryst D* **2011**, *67* (4), 355–367. https://doi.org/10.1107/S0907444911001314.
(87) Adams, P. D.; Afonine, P. V.; Bunkóczi, G.; Chen, V. B.; Davis, I. W.; Echols, N.; Headd, J. J.; Hung, L.-W.; Kapral, G. J.; Grosse-Kunstleve, R. W.; McCoy, A. J.; Moriarty, N. W.; Oeffner, R.; Read, R. J.; Richardson, D. C.; Richardson, J. S.; Terwilliger, T. C.; Zwart, P. H. PHENIX: A Comprehensive Python-Based System for Macromolecular Structure Solution. *Acta Cryst D* **2010**, *66* (2), 213–221. https://doi.org/10.1107/S0907444909052925.
(88) Chen, V. B.; Arendall, W. B.; Headd, J. J.; Keedy, D. A.; Immormino, R. M.; Kapral, G. J.; Murray, L. W.; Richardson, J. S.; Richardson, D. C. MolProbity: All-Atom Structure Validation for Macromolecular Crystallography. *Acta Cryst D* **2010**, *66* (1), 12–21. https://doi.org/10.1107/S0907444909042073.
(89) Heltweg, B.; Jung, M. A Homogeneous Nonisotopic Histone Deacetylase Activity Assay. *J Biomol Screen* **2003**, *8* (1), 89–95. https://doi.org/10.1177/1087057102239644.
(90) Niesen, F. H.; Berglund, H.; Vedadi, M. The Use of Differential Scanning Fluorimetry to Detect Ligand Interactions That Promote Protein Stability. *Nat Protoc* **2007**, *2* (9), 2212–2221. https://doi.org/10.1038/nprot.2007.321.